minerals

MDPI

Article

Upscaling Spectral Induced Polarization from Pore to Core Scale in Tight Reservoirs: A 3D Impedance Network Approach with an Improved Membrane Polarization Model

Tianqi Wang, Kui Xiang *, Xiaolong Tong * and Liangjun Yan

Key Laboratory of Exploration Technologies for Oil and Gas Resources, Yangtze University, Wuhan 430100, China; wtqyzu@163.com (T.W.); yljemlab@163.com (L.Y.)
* Correspondence: cjdxxk@163.com (K.X.); tongxl1988@hotmail.com (X.T.)

Abstract

Tight reservoirs exhibit complex pore structures and strong heterogeneity, which complicate reservoir characterization. Although spectral induced polarization (SIP) is sensitive to pore structure, existing polarization models are formulated at the pore scale and are difficult to connect with measurements across different core volumes. We adopted an improved membrane polarization model and coupled it with a three-dimensional impedance network to investigate two-stage SIP upscaling: from pore systems to core-scale networks, and from local core volumes represented by subnetworks to larger parent cores. The framework was used to determine the representative elementary volume (REV), evaluate subnetwork representativeness, examine fracture-controlled heterogeneity, and compare simulations with laboratory measurements. The results show that REV size is controlled by the distribution ranges of pore radius and pore length. Homogeneous networks converge with sufficient sampling, whereas subnetworks from strongly heterogeneous fractured cores may exhibit relative deviations exceeding tenfold when fracture structures are not adequately captured. Impedance network inversion can reproduce measured spectra, but the recovered pore distributions are non-unique and represent electrically equivalent structures. Laboratory-scale SIP data may not fully capture large-scale heterogeneity; integrating logging or imaging information may, therefore, help constrain cross-scale non-local effects and improve the reliability of comprehensive reservoir evaluation.

Keywords: tight reservoir; spectral induced polarization; impedance network; clay minerals; cross-scale upscaling

Check for updates

Academic Editor: Stanisław Mazur

Received: 16 June 2026
Revised: 21 July 2026
Accepted: 21 July 2026
Published: 23 July 2026

Copyright: © 2026 by the authors. Licensee MDPI, Basel, Switzerland. This article is an open access article distributed under the terms and conditions of the Creative Commons Attribution (CC BY) license.

1. Introduction

Tight reservoirs serve as important carriers of unconventional oil and gas resources and occupy an increasingly prominent position in the global energy structure. However, these reservoirs generally exhibit complex pore structures, low permeability, and strong heterogeneity, which pose significant challenges to reservoir characterization and fluid identification [1,2]. From a mineralogical perspective, the pore structures of tight reservoirs do not exist in isolation but rather are strongly controlled by mineral composition and diagenetic evolution. Different rock-forming minerals develop characteristic pore types and pore throat configurations during compaction, cementation, and dissolution, thereby determining the electrical transport properties of the reservoir [3,4]. These mineralogical effects can be summarized as follows. First, secondary quartz overgrowth or lattice expansion can reduce primary porosity and enhance local heterogeneity. Second, carbonate

cementation can reduce reservoir space, whereas carbonate dissolution can improve it. Third, clay minerals may clog pore throats, while their intercrystalline micropores can also provide important storage space and conductive pathways [5,6]. Traditional logging and seismic methods often suffer from insufficient resolution or limited sensitivity to fluids when evaluating such tight reservoirs with complex mineral-pore structures, which necessitates the development of new geophysical evaluation techniques. The induced polarization (IP) method in electrical exploration, particularly spectral induced polarization (SIP) technology, measures the complex resistivity response of rock samples or formations at different frequencies and can effectively reflect information on pore structure and fluid properties, having become one of the important geophysical evaluation means for reservoirs [7,8]. Numerous experimental studies indicate that induced polarization parameters exhibit significant correlations with key reservoir parameters such as hydraulic conductivity, specific surface area, and pore radius distribution [9–14], providing a theoretical basis for reservoir evaluation using induced polarization data.

Two primary polarization mechanisms govern induced polarization in porous media when metallic particles are excluded from consideration. The first is electrical double layer (EDL) deformation polarization. This theory posits that the polarization effect arises from charge separation within the electrical double layer (EDL) at mineral grain surfaces, particularly polarization induced by the tangential movement of counterions in the Stern layer [15–18]. The second is membrane polarization theory, first introduced by Marshall and Madden [19]. This theory attributes the polarization effect to narrow pore throats (narrow pores) in the pore space that exhibit selectivity toward ion transport, which leads to the formation and relaxation of ion concentration gradients under an applied electric field. Subsequent studies suggest that these two mechanisms may coexist and interact in natural reservoirs [20–23]. Recently, Kreith et al. [24] advanced the membrane polarization model by treating Stern layer cations as a third ionic species in the solution and assigning them a separate ion transport equation. By solving the coupled Poisson–Nernst–Planck equations, they computed the microscopic current density within pores, thereby more accurately describing the coupled polarization effects of the Stern and diffuse layers.

Although existing polarization models can effectively explain the physical mechanisms of induced polarization at the pore scale, actual induced polarization data are typically acquired at the core sample scale or field exploration scale, where the scales differ substantially from the pore scale. Existing polarization models cannot effectively interpret such data, and an effective method linking microscopic mechanisms to macroscopic induced polarization data is still needed. Pore network models have been widely applied to predict permeability, relative permeability, and electrical parameters in conventional and unconventional hydrocarbon reservoirs [25–28], to evaluate CO_2 injectivity and caprock integrity for geological CO_2 storage [29], and to study moisture transport in the vadose zone and contaminant remediation in groundwater [30]. Stebner et al. [31] and Maineult et al. [32] upscaled pore-scale spectral polarization responses using random pore network models, employing the membrane polarization model and the Pelton resistivity model [33], respectively. In these approaches, pore-scale units with different electrical or geometric parameters are connected through two-dimensional or three-dimensional network topologies, and the effective complex resistivity is obtained by solving Kirchhoff's equations at the network nodes. Their studies demonstrated that impedance networks can bridge microscopic pore-scale polarization mechanisms and macroscopic electrical dispersion, with the statistical distribution and connectivity of individual impedance elements exerting a major control on the bulk SIP response.

Building on these foundations, recent studies have further extended both the dimensionality of impedance network modeling and the range of materials investigated

by broadband SIP. Maineult et al. [34] used three-dimensional impedance networks to reproduce the complex resistivity spectra of sand–pyrite–water mixtures, showing that the abundance and spatial arrangement of polarizable components strongly influence the macroscopic response. In a complementary experimental study, Leroy et al. [35] combined broadband SIP measurements of low-pH cement and concrete with membrane- and Maxwell–Wagner-polarization models to relate the observed spectra to pore structure and interfacial electrochemical processes.

Complementary physics-based simulations have also been used to investigate the influence of mineral distribution and structural heterogeneity on induced polarization responses. Wu et al. [36], for example, conducted numerical simulations of submarine polymetallic sulfide deposits based on the Poisson–Nernst–Planck equations and systematically revealed the relationships between disseminated, vein-like, and massive mineralization structures and IP parameters. Although such physics-based simulations provide important insights into the relationship between structural heterogeneity and electrical responses, realistic upscaling also requires reliable characterization of pore and fracture geometries. In this context, recent microtomography (μCT)-based digital-core studies have advanced open-porosity prediction for standard core plugs using supervised machine learning models and have demonstrated the applicability of digital rock workflows to reservoir characterization and flow-related analyses in sandstone and carbonate reservoirs [37,38]. These developments indicate that image-derived structural information can provide valuable constraints for constructing more realistic pore network models. On this basis, determining the representative elementary volume (REV) is essential for ensuring that the constructed network adequately captures the structural features controlling macroscopic transport properties and that the simulation results are statistically representative [39,40]. The REV defines the minimum statistically representative scale, enabling simulations to adequately capture the connectivity features that govern macroscopic transport properties [41] and avoiding sampling bias and spurious results associated with sub-REV volumes [42]. In digital rock and pore network modeling, the REV serves as a critical bridge between microscopic pore structure and macroscopic property prediction [43,44], ensuring the reliability of upscaling electrical responses such as complex resistivity [45] while optimizing computational resource allocation through balancing resolution and representative volume [46].

In this study, we adopted an improved membrane polarization model and coupled it with a three-dimensional impedance network to investigate two-stage SIP upscaling: from individual pore systems to core-scale networks, and from local core volumes represented by subnetworks to larger parent cores. We determined the REV, evaluated subnetwork representativeness through repeated extraction, examined fracture-related spatial heterogeneity, and compared the numerical results with laboratory measurements of block and plug samples. This study further investigated how fracture-related heterogeneity affects the relationship between local and global SIP responses and assessed the non-uniqueness of impedance network inversion.

2. Materials and Methods

2.1. Membrane Polarization Model

Kreith et al. [24] built upon previous membrane polarization models, treated Stern layer cations as a third ionic species in the solution, and assigned them a separate ion transport equation. The equivalent ion concentrations in the Stern layer of wide and narrow pores c_S are, respectively:

$$c_S = \frac{2\Sigma_S}{Fr_1},\ \bar{c}_S = \frac{2\Sigma_S}{Fr_2} \tag{1}$$

where Σ_S is the Stern layer charge density; r_1 and r_2 are the wide and narrow pore radii, respectively; and F is the Faraday constant. By considering their ion transport and current continuity equations, the linearized Nernst–Planck equation for the Stern layer equivalent ions is as follows:

$$i\omega c_S = MD_S \frac{\partial^2 c_S}{\partial x^2} - \mu_S c_{S,0} \frac{\partial^2 U}{\partial x^2} \tag{2}$$

$$M = 1 + \frac{\kappa \Sigma_S}{2Fc_\infty \cosh\left(\frac{e\psi_d}{2k_B T}\right)} \tag{3}$$

where D_S and μ_S are the Stern cation diffusion coefficient and mobility, respectively; $c_{S,0}$ is the equilibrium Stern layer concentration; M is the interlayer coupling coefficient [47]; U is the axial electric potential; κ is the inverse Debye length; k_B is the Boltzmann constant; ψ_d is the electric potential at the Stern layer; and c_∞ is the bulk solution concentration.

Under this assumption, the Poisson equation accounting for cations c_p, anions c_n, and Stern layer ions is given by:

$$\frac{\partial^2 U}{\partial x^2} = \frac{F}{\epsilon_0 \epsilon_r}(c_p - c_n + c_S) \tag{4}$$

where ϵ_0 and ϵ_r are the vacuum permittivity and relative permittivity, respectively. By solving the coupled Poisson–Nernst–Planck equations, we can calculate the microscopic current density at each point within the pore. Incorporating boundary conditions, integrating over the pore length and dividing by the terminal voltage yields the impedance of the one-dimensional pore sequence:

$$Z(\omega) = \frac{V}{I} = \frac{2(L_1 + L_2)}{\int_{-L_1}^{L_1} J_1(x,\omega)dx + a\int_{-L_2}^{L_2} J_2(x,\omega)dx} \cdot \frac{1}{\pi r_1^2} \tag{5}$$

For a wide-and-narrow pore system of length $2(L_1 + L_2)$ and matrix cross-sectional area A_S, the effective resistivity is given by [48]:

$$\rho_{\text{eff}} = Z(\omega) \cdot \frac{A_S}{L} \tag{6}$$

The impedance response obtained for a single wide-and-narrow pore system was subsequently used as the elementary impedance component for constructing the pore combination (PC) units described in Section 2.2.

2.2. Impedance Network Model

The three-dimensional impedance network was constructed to upscale the pore-scale membrane polarization response to the core scale through spatial topological connections. In the network, each edge connecting two adjacent nodes was represented by a pore combination (PC) unit. Different PC units could be assigned different pore-geometric parameters to characterize the spatial heterogeneity of the rock pore structure.

Each PC unit consisted of n identical wide-and-narrow pore systems connected in series. Figure 1 shows the geometry of one wide-and-narrow pore system. A single system comprises two wide pore segments connected by a central narrow pore segment. Each wide pore segment has a radius r_1 and a length L_1, giving a total wide pore length of $2L_1$. The central narrow pore segment has a radius r_2 and a total length of $2L_2$. Therefore, the total length of one wide-and-narrow pore system is:

$$L_{sys} = 2L_1 + 2L_2 = 2(L_1 + L_2) \tag{7}$$

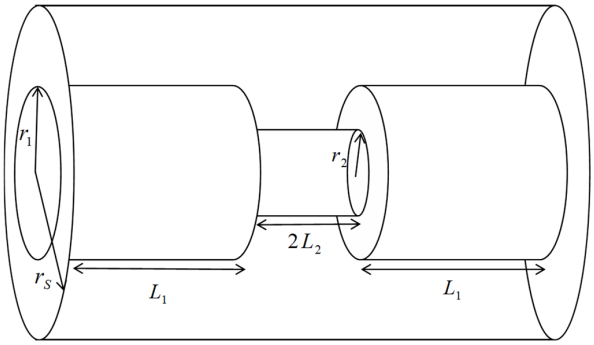


Figure 1. A single wide-and-narrow pore system. Each PC unit consists of n identical wide-and-narrow pore systems connected in series.

Here, r_1 represents the pore body radius, whereas r_2 represents the pore throat radius. The geometric parameters of the wide and narrow pore segments are related through the proportional coefficients f_K and f_L, respectively:

$$r_1 = r_2 f_K,\ L_1 = L_2 f_L \tag{8}$$

The n wide-and-narrow pore systems within the same PC unit have identical values of r_1, r_2, L_1, and L_2, whereas these parameters may differ among PC units. In this way, each PC unit represents one specific pore type, and the assignment of different PC units to the network edges represents the pore structure heterogeneity of the rock.

Each PC unit was embedded in a non-conductive cylindrical matrix with a radius $r_S = f_S f_K r_{2\max}$. The total length of a PC unit, L_{total}, was defined by the distance between two adjacent network nodes. The n wide-and-narrow pore systems occupy a total length of nL_{sys}. When L_{total} is not an integer multiple of L_{sys}, the remaining length L_{rem} is given by $L_{total} = nL_{sys} + L_{rem}$.

The residual segment was assigned the same wide pore radius as the series-connected systems. Its nominal narrow pore radius was also set equal to r_1, so that this segment behaved as an approximately uniform pore and did not introduce an additional polarization response.

The equivalent impedance of each PC unit was obtained by combining the impedances of the n identical wide-and-narrow pore systems and the residual segment in series. The resulting complex conductivity was then assigned to the corresponding edge of the three-dimensional network. Figure 2 illustrates the network topology, in which every connection between adjacent nodes represents one PC unit.

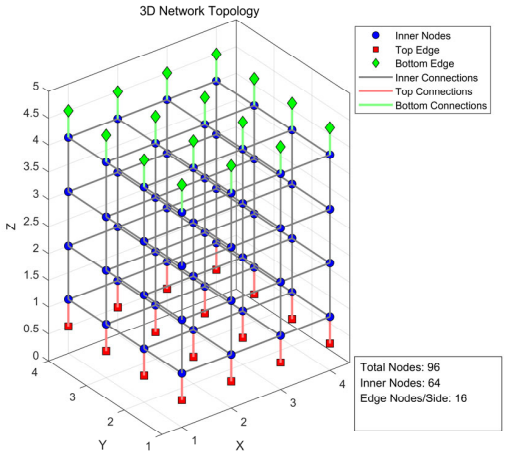


Figure 2. Schematic of the impedance network model with a network size of 4.

For a three-dimensional cubic network with $l \times l \times l + 2$ nodes, the network size is defined as l, the total number of internal nodes is $n = l^D$, and the total number of impedance units connecting these nodes is $m = Dl^D - l^{(D-1)}(D-2)$. Each node is connected to its adjacent nodes through PC units. Let the complex electric potential at node (i, j, k) be $V^*_{i,j,k}$ and the complex current flowing through the PC unit connecting nodes (i, j, k) and $(i+1, j, k)$ be:

$$I^*_{(i,j,k)\to(i+1,j,k)} = \sigma^*_{(i,j,k)\to(i+1,j,k)}(V^*_{i,j,k} - V^*_{i+1,j,k})\frac{\pi r_s^2}{L_{total}} \tag{9}$$

where $\sigma^*_{(i,j,k)\to(i+1,j,k)}$ is the complex conductivity of this PC unit, calculated from the membrane polarization model. We applied Kirchhoff's current law to each internal node, such that the sum of complex currents flowing into the node equals zero:

$$\sum_{\text{adj}} I^* = 0 \tag{10}$$

From this, a system of linear equations for the complex potentials of all nodes can be established:

$$\begin{pmatrix} \sum_i \sigma_{1,i} & \cdots & 0 \\ \vdots & \ddots & \vdots \\ 0 & \cdots & \sum_k \sigma_{n,k} \end{pmatrix} \begin{pmatrix} V_1 \\ \vdots \\ \vdots \\ V_n \end{pmatrix} = \begin{pmatrix} V_{in}\sigma_{1,in} \\ \vdots \\ \vdots \\ V_{out}\sigma_{n,out} \end{pmatrix} \tag{11}$$

$$D^* \cdot \mathrm{V}^* = b^* \tag{12}$$

where D* is the sparse matrix of complex coefficients, V* is the vector of complex electric potentials at the nodes, and b^* follows from the boundary conditions. We applied fixed voltages V_{in} and V_{out} to the upper and lower boundaries, respectively, with zero current at the lateral boundaries. After solving this linear system in MATLAB R2021a to obtain the potentials at all nodes, we calculated the total complex current through the boundaries and then obtained the effective complex resistivity $\rho^*_{\text{net}}(\omega)$ of the entire network.

3. Results

3.1. Representational Capacity and Parameter Sensitivity of Random Impedance Network Models

3.1.1. Single Pore Type Verification

To validate upscaling within the impedance network framework, we simulated a network of size 24 containing only a single pore type (Figure 3). The network output matches the analytical membrane polarization solution for that pore type exactly. Across 100 iterative calculations, the relative difference between the two approaches at each frequency was less than 1×10^{-8} percent. Such agreement demonstrates that impedance network simulation reliably captures pore-scale upscaling in a fully homogeneous medium.

At the single-pore scale, the membrane polarization response is independently controlled by two geometric parameters—pore radius and pore length—and there exists a clear quantitative mapping relationship. With a fixed pore length and varying narrow pore radius r_2, the phase peak changes non-monotonically with pore radius: when r_2 is on the nanometer-to-submicron scale, the pore throat size is comparable to the electric double layer thickness, cation-selective transport is strong, and the polarization intensity can reach tens of mrad; whereas when r_2 increases to the micron scale or above, the EDL proportion drops sharply, and the phase peak rapidly decreases to less than 1 mrad (Figure 4a). With a fixed pore radius and varying narrow pore length L_2, the characteristic frequency f_c (the frequency corresponding to the phase peak) is controlled by the ion diffusion relaxation time: short pore lengths correspond to high-frequency polarization, and long pore lengths

correspond to low-frequency polarization (Figure 4b). The typical pore throat radii in tight reservoirs are distributed between 10^{-9} and 10^{-6} m, and the pore lengths are distributed between 10^{-7} and 10^{-4} m, which fall exactly within the strong polarization window, giving membrane polarization a detectable response amplitude and characteristic frequencies within the SIP band; whereas the pore throat scales of conventional high-porosity and high-permeability sandstones or unconsolidated media are far larger than the EDL thickness, and the membrane polarization contribution approaches zero.

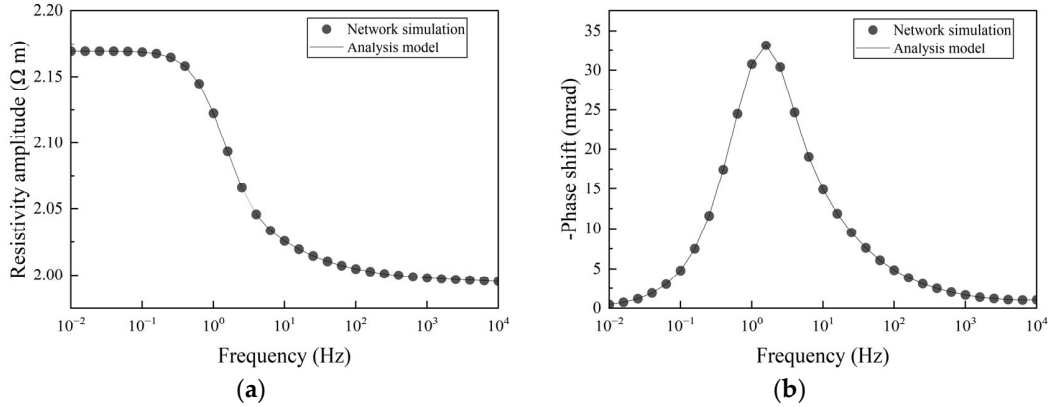


Figure 3. Simulated complex resistivity spectrum for a network of size 24. (**a**) Resistivity amplitude; (**b**) phase angle. Contains only one pore type (r_2 = 0.2 μm, L_2 = 2 μm). Points are network simulation results, and the curve is the analytical solution of the membrane polarization model for a single pore type.

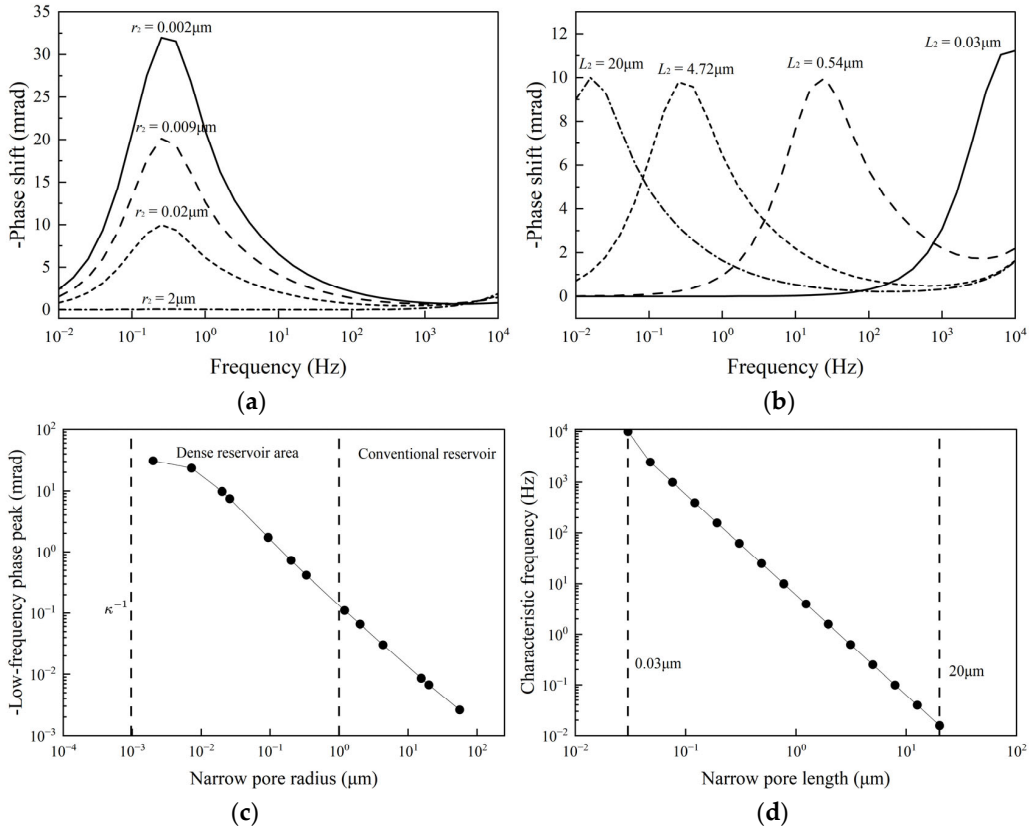


Figure 4. Panels (**a**,**c**) show how the single-pore low-frequency phase peak varies with narrow pore radius, and κ^{-1} is the Debye length; panels (**b**,**d**) show how the single-pore characteristic frequency varies with narrow pore length.

We adopted the surface complexation model [49–51] to calculate the Stern layer charge density and surface charge distribution coefficient on pore surfaces. Under 0.1 mol/L neutral NaCl solution conditions, the electrochemical parameters calculated using the SCM are listed in Table 1. Different electrochemical parameter inputs primarily alter the simulated resistivity magnitude and phase magnitude (Figure 5), whereas the characteristic frequency is insensitive to changes in electrochemical parameters. The higher surface charge density resulting from the high specific surface area of clay minerals reduces the simulated resistivity magnitude and enhances the polarization response.

Table 1. Electrochemical parameters of two surface minerals.

Surface Minerals	Σ_S (C/m^2)	ψ_d (V)	f_Q
Montmorillonite	0.11215	−0.051145	0.74770
Quartz	0.049687	−0.041316	0.59483

f_Q is Partition coefficient.

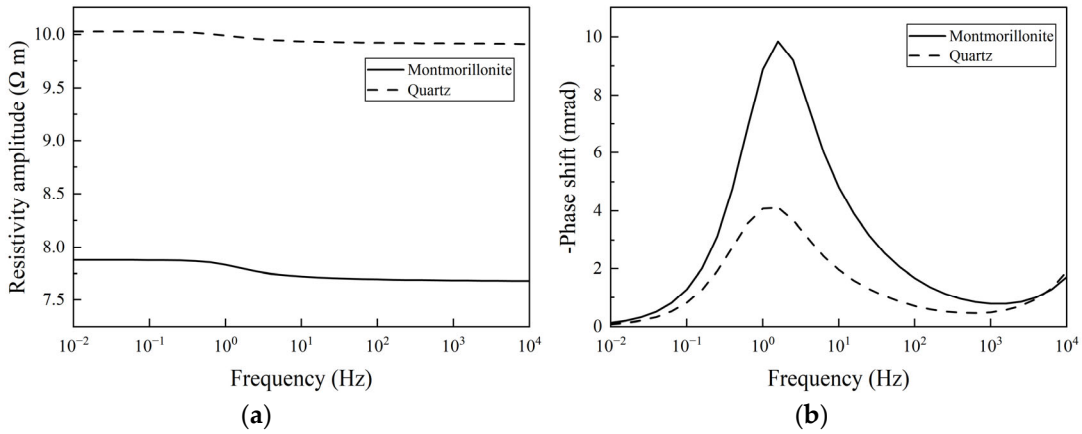


Figure 5. (**a**) Variations in the resistivity magnitude of a single pore under different electrochemical parameters. (**b**) Variations in the phase of a single pore under different electrochemical parameters.

3.1.2. Upper and Lower Bounds of Representational Capacity for Multiple Pore Types

We added additional pore types to characterize the broad ranges of pore throat radii and pore lengths present in natural tight reservoirs. In such reservoirs, differences in pore throat radius and pore length span 2–3 orders of magnitude; this heterogeneity was represented by connecting PC units with different pore radii and pore lengths in series and in parallel within the impedance network.

The pore radius distribution exerts significant control over the network polarization intensity. Numerical experiments with fixed pore length and varying pore radius (Figure 6) indicate that wide pores form low-resistance preferential conduction pathways, producing a significant electrical short-circuit effect on the high polarization contribution from narrow pores. The effective polarization intensity of the network exhibits well-defined upper and lower bounds: the upper bound approaches the pure narrow pore response, whereas the lower bound is suppressed by the conductive dominance of wide pores. When the network simultaneously contains narrow pores with r_2 = 0.002 μm and wide pores with r_2 = 0.2 μm, the effective phase magnitude is significantly lower than the linear average of the analytical solutions for the two pore types and decays monotonically as the proportion of narrow pores decreases. As the pore radius difference decreases (Figure 7), the impedance contrast among individual branches diminishes, and the network response gradually converges toward the arithmetic average. The extreme values of the pore radius distribution—particularly whether the minimum pore radius falls within the mem-

brane polarization-dominated regime—determine the range of variation of the network polarization intensity.

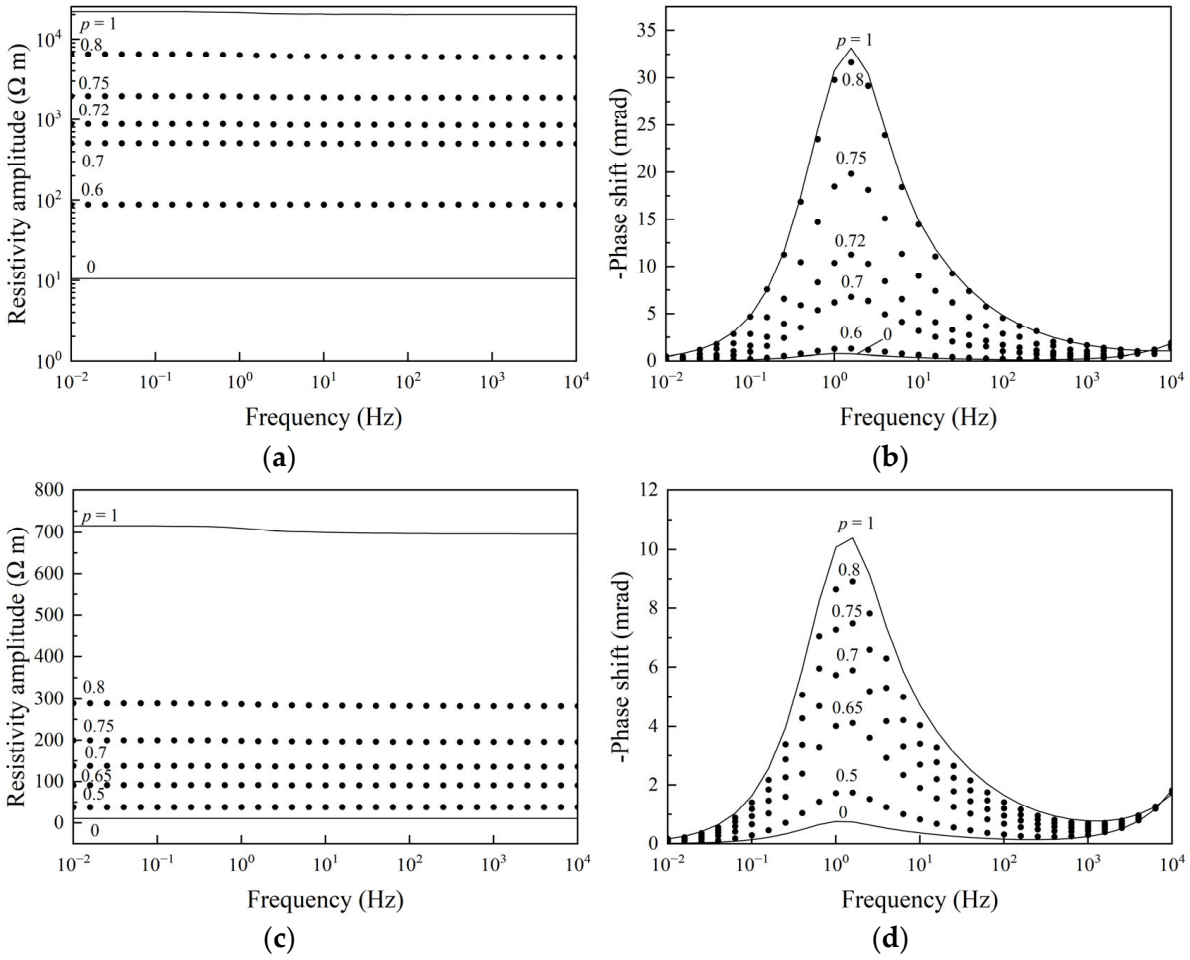


Figure 6. Complex resistivity spectra of a network with size 24 under different pore type proportions, with fixed pore length. The network contains two pore types [(**a**,**b**) correspond to r_2 = 0.002 μm, L_2 = 2 μm and r_2 = 0.02 μm, L_2 = 2 μm; (**c**,**d**) correspond to r_2 = 0.02 μm, L_2 = 2 μm and r_2 = 0.2 μm, L_2 = 2 μm]. p denotes the proportion of the narrower-throat pore type relative to the total pore volume of the network.

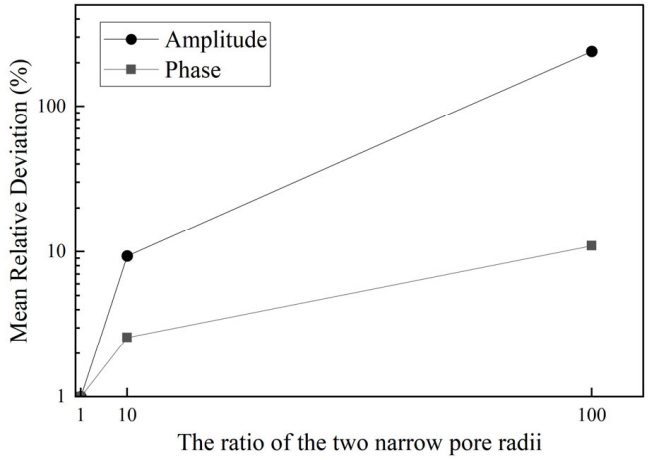


Figure 7. Relative changes in the average value of the membrane polarization analytical model and the network simulation amplitude and phase at p = 0.5 under different pore throat ratios for two pore types.

The frequency bounds of the network phase spectrum are strictly constrained by the extreme values of the pore length distribution: the high-frequency upper bound is determined by $L_{2,min}$, and the low-frequency lower bound is determined by $L_{2,max}$. The network is equivalent to connecting different numbers of polarization units in series; because the polarization intensity of each unit is identical, the effective response manifests as the arithmetic average of the analytical solutions for each pore type (Figure 8b,d). Short pore lengths produce high-frequency phase peaks, whereas long pore lengths produce low-frequency phase peaks; under a broad distribution, the overall phase spectrum exhibits characteristics of multiple-peak superposition or broadband spreading, consistent with the measured SIP spectra of tight rocks. Numerical experiments indicate that when the number of pore types v = 10, continuing to increase the discretization number to v = 1000 has a negligible effect on the effective network response (Figure 8b,d), which indicates that as long as the statistical range of the pore length distribution is fixed, the coverage range of the network characteristic frequencies tends to stabilize.

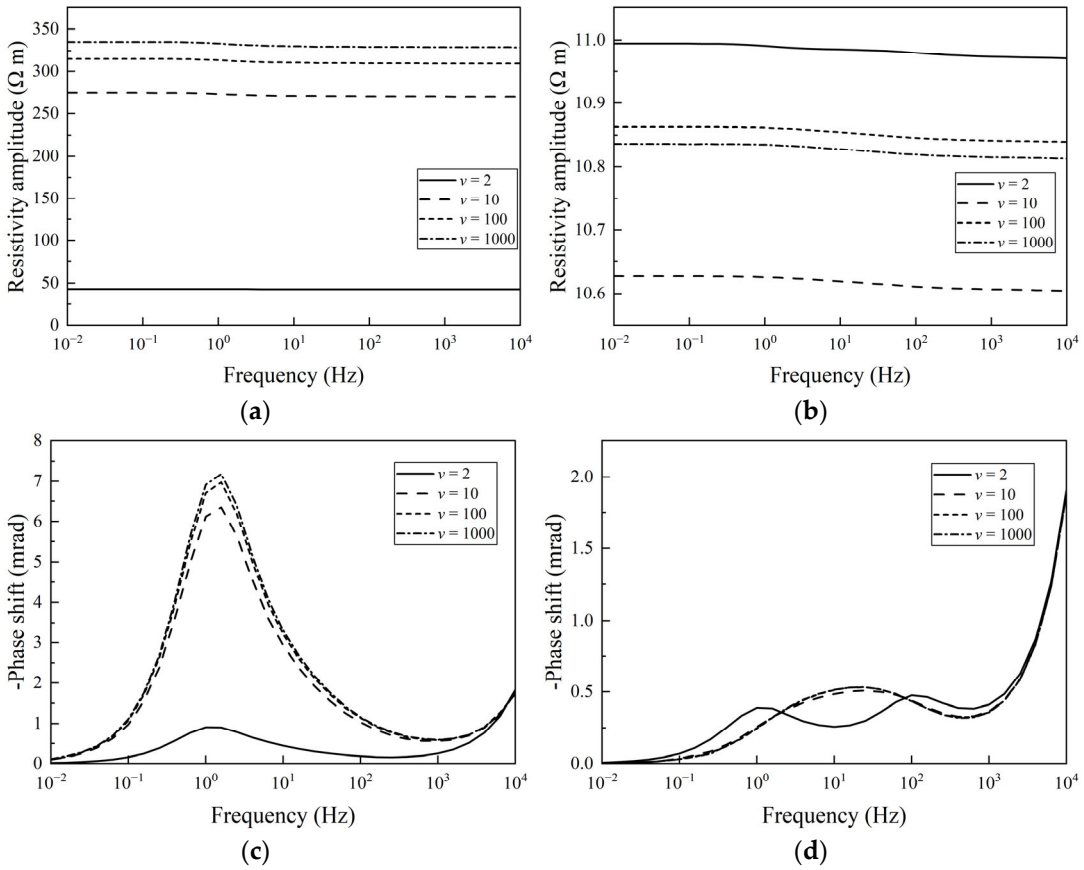


Figure 8. Complex resistivity spectra for different numbers of pore types in a network of size 24. Numbers of pore types v = 2, 10, 100, and 1000 are generated using a logarithmic equal-interval distribution, with each pore type having the same proportion in the network. Panels (**a**,**c**) are for fixed pore length: $r_{2,min}$ = 0.002 μm, $r_{2,max}$ = 0.2 μm, L_2 = 2 μm. Panels (**b**,**d**) are for fixed pore cross-sectional area: $L_{2,min}$ = 0.08 μm, $L_{2,max}$ = 2 μm, r_2 = 0.2 μm.

When the pore radius distribution range is fixed, the complex resistivity spectrum of the network converges to the analytical solution of an equivalent single pore type as the number of pore types v increases (Figure 8a,c), with the equivalent narrow pore radius being approximately 0.0288 μm. This equivalent radius is neither the arithmetic mean nor the geometric mean but rather represents an overall statistical property of the network arising from the competition between the short-circuit effect of wide pores and

the polarization contribution of narrow pores; its physical meaning likely corresponds to a characteristic scale weighted by polarization intensity under a log-uniform pore radius distribution. Provided that the statistical range of the pore radius and pore length distribution is fixed, the network response exhibits a definite equivalent characteristic, and increasing the number of pore types indefinitely is unnecessary; the range of variation in the overall response is strictly bounded by the geometric extreme values.

The representational capacity of random impedance networks is strictly bounded by the network geometric parameters (Figure 9). The geometric parameters defining these upper and lower bounds are listed in Table 2. For induced polarization response curves falling within the representable range, the impedance network can achieve effective characterization by connecting different pore types in series and in parallel. Changing geometric parameters and electrochemical inputs can expand or narrow this range. The above upper and lower bounds are calibrated based on clay mineral electrochemical parameters and need to be re-determined in combination with specific mineral compositions in practical applications. This study focuses primarily on the influence of geometric parameters on scale effects.

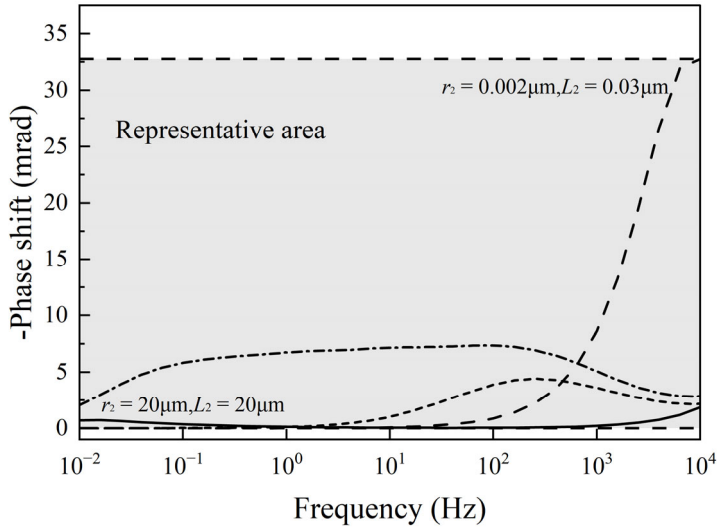


Figure 9. The gray region in the figure represents the representable range of the random impedance network model; this range is bounded by two sets of geometric parameters at the opposite ends of the diagonal.

Table 2. Geometric parameters defining the upper and lower bounds of the representable range in Figure 9.

Symbol	Description	Value
$r_{2,\min}$	Lower bound of narrow pore radius (m)	2.00×10^{-9}
$r_{2,\max}$	Upper bound of narrow pore radius (m)	2.00×10^{-5}
$L_{2,\min}$	Lower bound of narrow pore length (m)	3.00×10^{-8}
$L_{2,\max}$	Upper bound of narrow pore length (m)	20.00×10^{-6}
f_K	Pore size scaling factor	10
f_L	Pore length scaling factor	9
f_S	Matrix scaling factor	1.1
L_{total}	Node spacing (m)	4.00×10^{-4}

3.2. Numerical Simulation of Induced Polarization Responses at Different Scales

3.2.1. Representative Elementary Volume of the Random Impedance Network Model

To determine the representative elementary volume (REV) size of the impedance network, we constructed cubic impedance networks of different sizes and selected v = 100 and v = 1000 for the number of pore types. The pore types were generated following a log-normal distribution in the pore radius and pore length parameter space, with each pore type having an equal probability of occurrence in the network, to simulate the statistical characteristics of the pore structure of actual samples. The mesh parameters used for the network simulations are listed in Table 3.

Table 3. Parameters used for the impedance network. A narrower distribution interval relative to Table 2 was adopted to simulate the influence of geometric parameters on convergence.

Symbol	Description	Value
D	Network dimension	3
l	Network size	4, 6, 8, . . ., 24
v	Number of pore types	100, 1000
$r_{2,\min}$	Lower bound of narrow pore radius (m)	2.00×10^{-9}
$r_{2,\max}$	Upper bound of narrow pore radius (m)	2.00×10^{-7}
$L_{2,\min}$	Lower bound of narrow pore length (m)	8.00×10^{-8}
$L_{2,\max}$	Upper bound of narrow pore length (m)	2.00×10^{-6}
f_K	Pore size scaling factor	10
f_L	Pore length scaling factor	10
f_S	Matrix scaling factor	1.1
L_{total}	Node spacing (m)	1.00×10^{-4}

To quantify the statistical stability and size dependence of the simulated SIP responses, we calculated the full-band coefficients of variation of resistivity magnitude and phase, $\overline{CV}_\rho(l_i)$ and $\overline{CV}_\phi(l_i)$, respectively, together with the relative changes in resistivity magnitude and phase between two consecutive network sizes, $\delta_\rho(l_i)$ and $\delta_\phi(l_i)$, respectively. Detailed definitions of these statistical quantities are provided in Appendix A.

Based on the above statistics, the REV size was defined as the minimum network size that simultaneously satisfied two criteria. First, $\overline{CV}_\rho(l_i)$ and $\overline{CV}_\phi(l_i)$ had to be lower than ε_{CV}, indicating adequate statistical stability among repeated realizations. Second, $\delta_\rho(l_i)$ and $\delta_\phi(l_i)$ had to be lower than ε_δ, indicating that a further increase in network size produced only limited changes in the macroscopic response.

Through 10 iterative computations for different network sizes with v = 100 and v = 1000 (Figure 10), the coefficient of variation between iterations and the relative change rate between sizes generally decrease with increasing network size. When the number of pore types v is small, the larger dispersion in the pore radius distribution results in a slower decay of the network response coefficient of variation with size, and the corresponding REV size is larger. When v = 1000, the network simulation convergence accelerates. Considering that stricter thresholds (e.g., 1%) in network calculations would significantly increase the REV size (l > 20) and computational cost, we adopted 5% as the threshold for each criterion for REV size determination (Figure 11). A threshold of 5% is already significantly lower than the typical systematic error of core-scale SIP measurements and the noise level of field exploration; the REV sizes determined thereby for v = 100 and v = 1000 are l = 14 and l = 10, respectively.

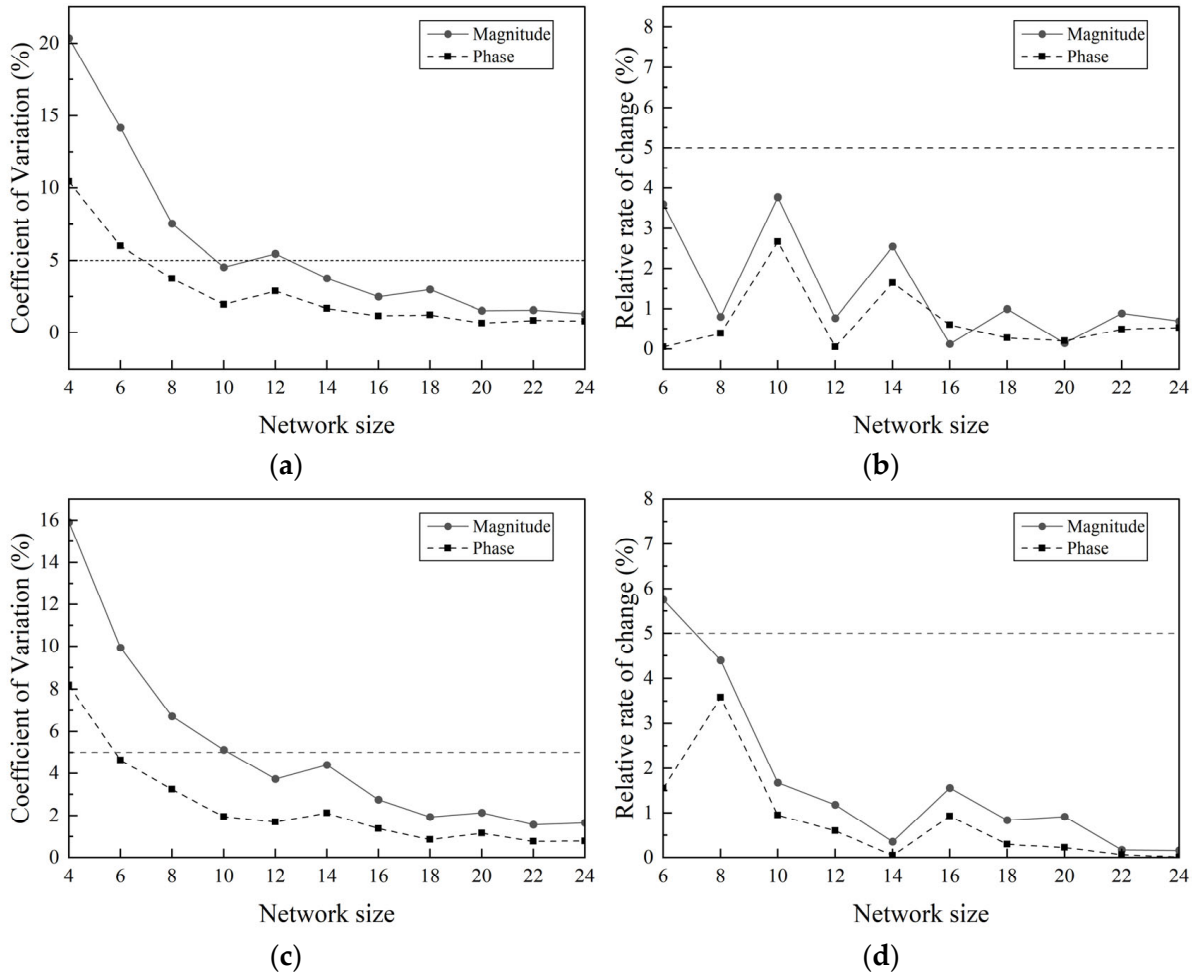


Figure 10. Coefficient of variation between cycles and relative change between sizes for amplitude and phase at different network sizes [(**a**,**b**) show results for v = 100 network, (**c**,**d**) show results for v = 1000 network]. Different network sizes use the same set of log-normally distributed pore types, with equal extraction probability for each pore type.

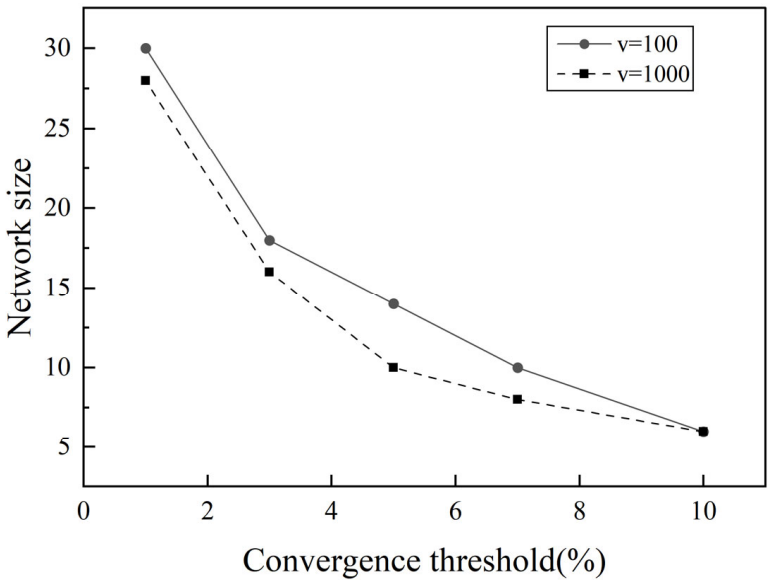


Figure 11. REV size of the random impedance network model under different thresholds.

Expanding the distribution ranges of pore length and pore radius causes the REV sizes corresponding to both pore type numbers to increase dramatically (Figure 12). The REV size that strictly satisfies the discrimination criterion is approximately 24. For rock samples with different degrees of pore distribution complexity, impedance networks of appropriate sizes should be selected to ensure the statistical stability and size independence of the simulated responses.

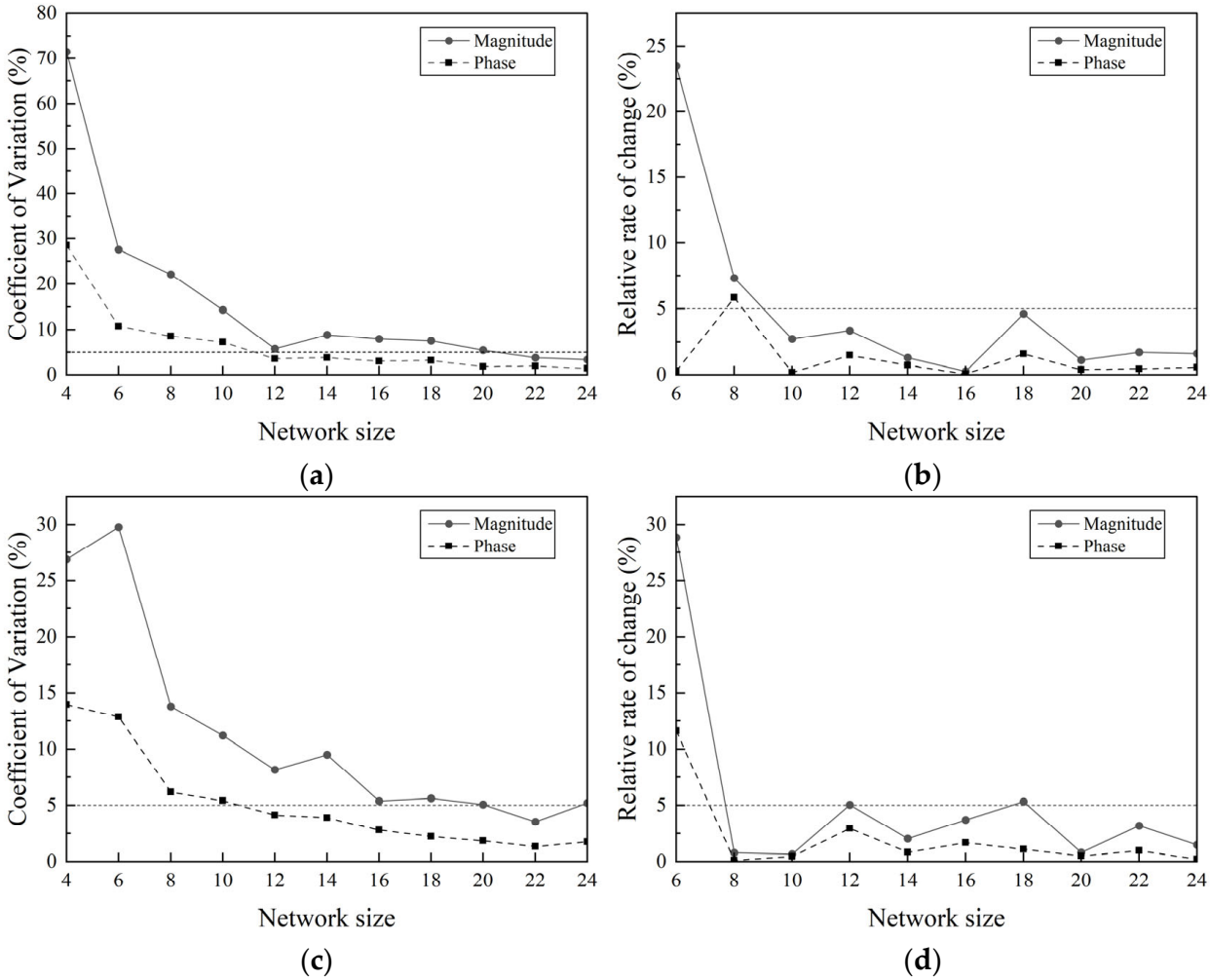


Figure 12. Inter-cycle coefficient of variation and inter-size relative rate of change for magnitude and phase across different network sizes with expanded pore radius and length distribution intervals relative to Figure 10 [(**a**,**b**): v = 100 network; (**c**,**d**): v = 1000 network].

The REV size is primarily controlled by the ranges of pore radius and pore length—that is, the degree of heterogeneity in porous media—rather than by the number of pore types. Expanding the pore radius and pore length distribution ranges (Table 4) yields an REV size of approximately l = 24, which is substantially larger than the REV size under the parameters in Table 3, indicating that the complexity of the pore distribution is the primary factor controlling the REV size. Within a fixed distribution range, the number of pore types primarily affects the convergence rate of the REV, with little effect on the REV size. Under the parameters in Table 3, the REV size for v = 1000 is four network-size units smaller than that for v = 100.

Table 4. Expanded output parameter range relative to the impedance network in Figure 10.

Symbol	Description	Value
D	Network dimension	3
l	Network size	4, 6, 8, . . ., 24
v	Number of pore types	100, 1000
$r_{2,\min}$	Lower bound of narrow pore radius (m)	2.00×10^{-9}
$r_{2,\max}$	Upper bound of narrow pore radius (m)	2.00×10^{-5}
$L_{2,\min}$	Lower bound of narrow pore length (m)	8.00×10^{-8}
$L_{2,\max}$	Upper bound of narrow pore length (m)	18.00×10^{-6}
f_K	Pore size scaling factor	10
f_L	Pore length scaling factor	10
f_S	Matrix scaling factor	1.1
L_{total}	Node spacing (m)	4.00×10^{-4}

3.2.2. Representativeness of Subnetworks in Random Impedance Networks

After determining an impedance network sufficiently representative of a rock sample, we expanded this network beyond the REV size and performed partial extraction to analyze the relationship between the SIP response of a partial sample and the whole at the core scale. The specific procedure was as follows: we constructed a sufficiently large parent network and solved for its simulated SIP response; subsequently, we extracted multiple subnetworks of different sizes from it and solved for their responses; finally, we conducted a comparative analysis of the simulated SIP responses, pore type distributions, and parameters of the subnetworks against those of the parent network.

Parent networks with network size 30 and pore type numbers of 100 and 1000 were selected, with the pore type distributions consistent with those in Figure 10. From these, subnetworks with sizes of 4, 6, 8, 10, 12, and 14 were extracted 10 times each (Figure 13). The results indicate that the convergence rate of subnetworks from parent networks with a larger number of pore types is significantly accelerated. Under the random assignment mode, the connectivity relationships among pore types in the network have limited influence on subnetwork representativeness; the convergence of subnetworks primarily depends on the statistical sufficiency of the pore types they contain (Figure 14). The deviation of subnetworks of different sizes relative to the parent network stems from whether the distribution of extracted pore types within the subnetwork is uniform, that is, the statistical similarity between the subnetwork and the parent network. Because each pore type occurs with smaller frequency in the v = 1000 network, subnetworks of the same size can encompass richer pore type information, and their convergence is superior to that of the v = 100 network.

To quantitatively evaluate the influence of microscopic heterogeneity on subnetwork representativeness, we introduced a dimensionless microscopic heterogeneity parameter, η, based on the local variation in pore throat radii around a set of mutually nonadjacent nodes. A larger value of η indicates stronger microscopic heterogeneity around these independent nodes. The detailed definition of η is provided in Appendix B.

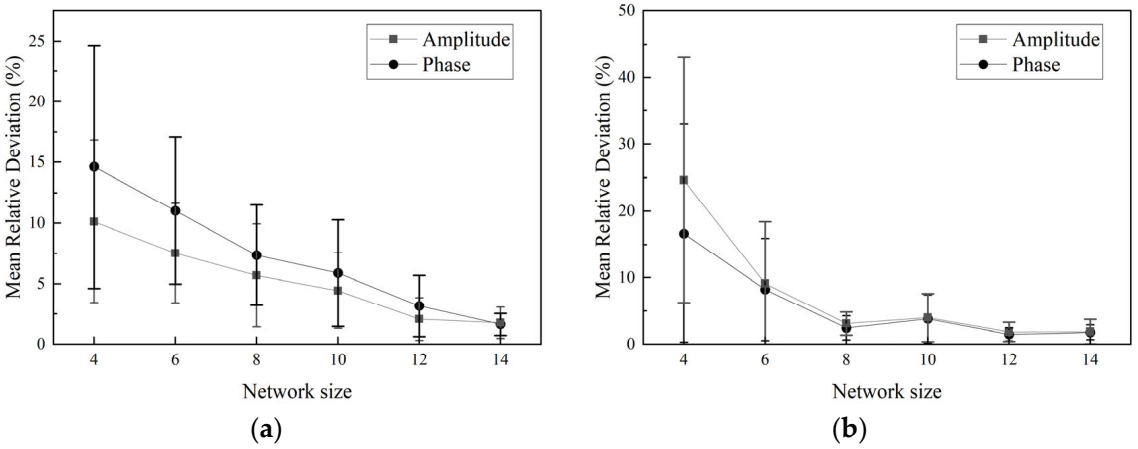


Figure 13. Subnetworks of different sizes extracted from two parent networks with v = 100 and v = 1000. (**a**) Average relative deviation of SIP responses between the parent network (v = 100) and its subnetworks; (**b**) average relative deviation of SIP responses between the parent network (v = 1000) and its subnetworks.

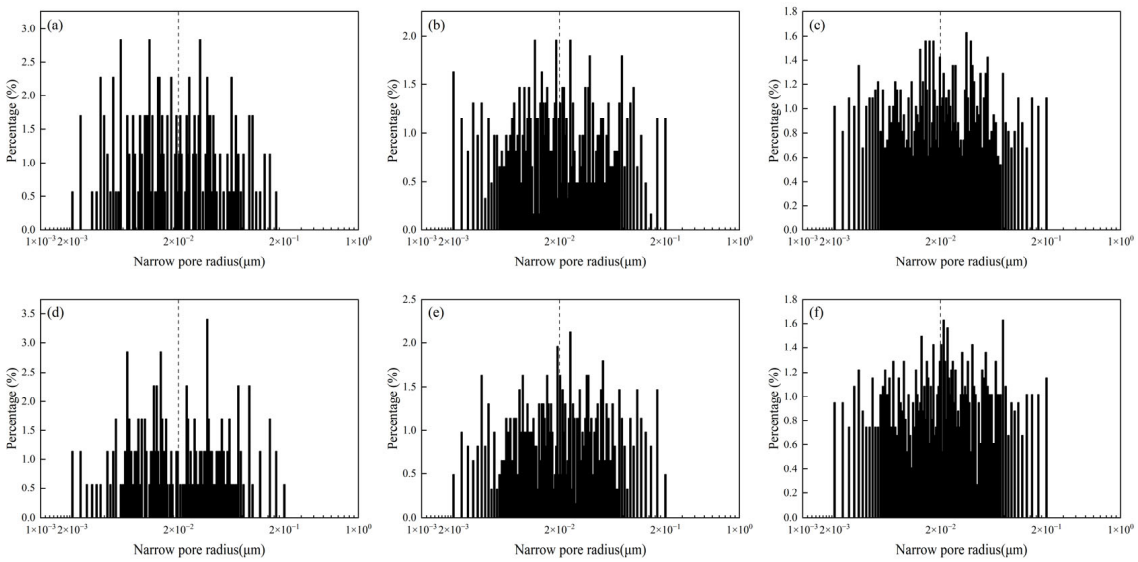


Figure 14. Pore throat distributions of subnetworks with network sizes 4, 6, and 8 in the parent network with v = 100 in Figure 13. Panel (**a**) shows the pore throat distribution of the subnetwork with the maximum deviation from the parent network SIP response among the 10 subnetworks with network size 4; (**d**) shows the pore throat distribution of the subnetwork with the minimum deviation from the parent network among these 10 subnetworks. Panels (**b**,**c**) show the pore throat distributions of the maximum- and minimum-deviation subnetworks for network size 6; (**e**,**f**) show the pore throat distributions of the maximum- and minimum-deviation subnetworks for network size 8.

Under the random assignment mode, the subnetwork representative size is insensitive to the microscopic heterogeneity parameter η; five networks with different values of η exhibited similar SIP responses (Figure 15). The simulated annealing algorithm optimization forms local large-pore/small-pore clusters (Figure 16); however, because the node positions still followed random assignment, the subnetwork representative sizes remained similar to those of completely random networks (Figure 17). Such microscopic heterogeneity is homogenized at the core scale, and the subnetwork representative size remains consistent with that of completely random networks. Whether a subnetwork is representative is determined by statistical sampling sufficiency rather than by local microscopic fluctuations.

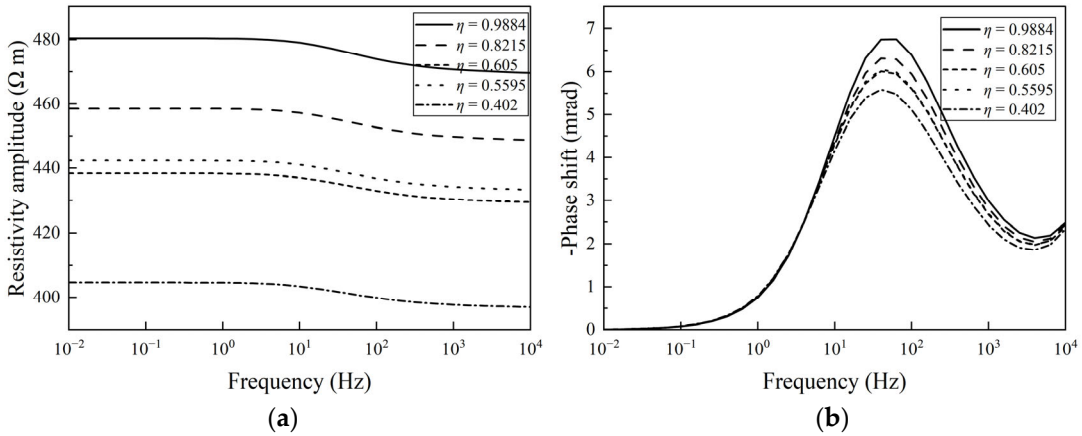


Figure 15. Simulated SIP responses of an impedance network with a network size of 31 and 100 pore types under different heterogeneity parameters: (**a**) resistivity magnitude and (**b**) phase. The network parameters used are the same as in Table 3.

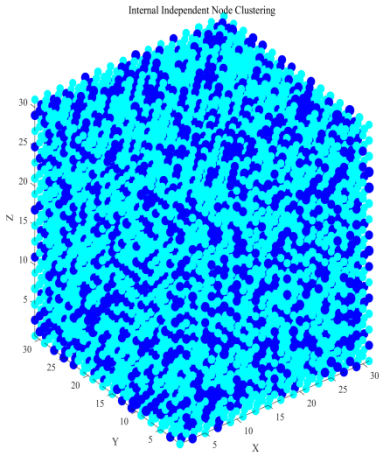


Figure 16. Optimization effect of the η = 0.605 network in Figure 15. Different colors represent different classes. The optimization algorithm divides the network into two classes: large-pore clusters and small-pore clusters.

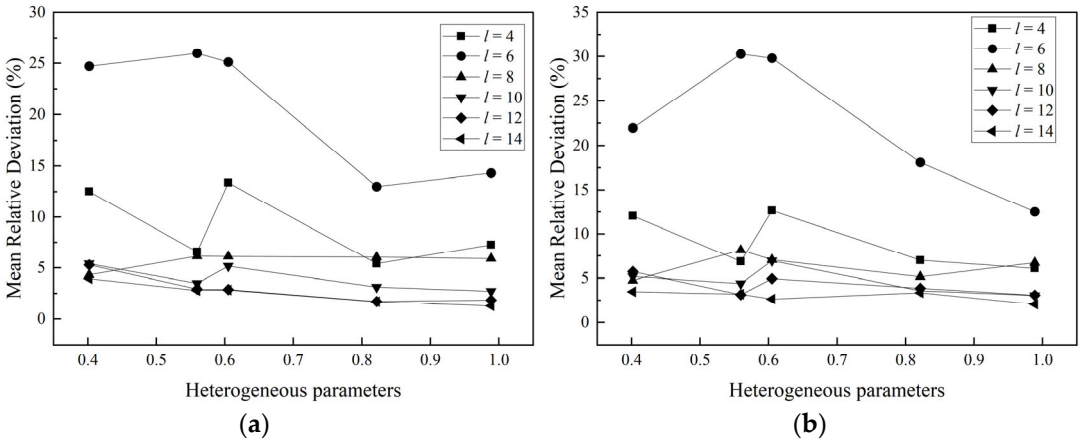


Figure 17. Mean relative deviation of subnetworks of different sizes from the parent network in Figure 15. Panel (**a**) shows the resistivity amplitude; (**b**) shows the phase peak. Each subnetwork was extracted 10 times.

3.2.3. Influence of Core-Scale Heterogeneity on Subnetwork Representativeness

The microscopic heterogeneity parameter η characterizes the local variation in pore throat radii around independent nodes but does not describe the large-scale spatial ar-

rangement or long-range correlation of pore structures. Therefore, it cannot characterize directional aggregation features such as connected fractures. To achieve heterogeneity at larger scales, this section controlled the spatial distribution of individual nodes through a clustering algorithm, simulating two states: fractures along the measurement direction and fractures perpendicular to the measurement direction (Figure 18). The clustering algorithm divides the network into two classes of individual nodes: fractures as large-pore clusters and the remainder as narrow-pore clusters. The SIP response of networks with fractures along the measurement direction is completely dominated by wide-pore fractures; the response of randomly distributed networks lies between those of the two fracture networks.

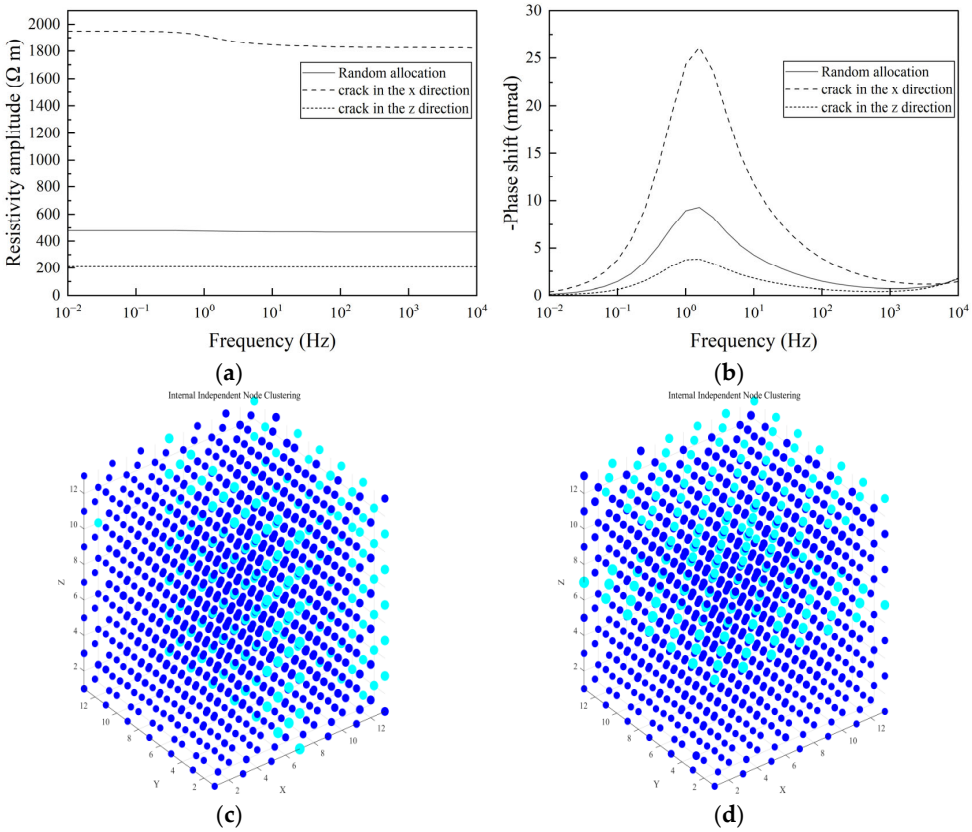


Figure 18. Simulated SIP responses (**a**,**b**) and clustering effects (**c**,**d**) for impedance networks with different spatial pore configurations, with a network size of 13 and 100 pore types. Dark-blue and cyan nodes represent the small-pore and large-pore/fracture-node classes, respectively. For the fracture network along the measurement direction, the average narrow pore radius r_2 range of independent nodes in the large-pore aggregation class is [0.07015, 0.12751] μm; in the small-pore aggregation class, r_2 is [0.00738, 0.0373] μm, and the microscopic heterogeneity parameter is η = 0.4959; for the fracture network perpendicular to the measurement direction, the average narrow pore radius r_2 range of independent nodes in the large-pore aggregation class is [0.0672, 0.12786] μm; in the small-pore aggregation class, r_2 is [0.00786, 0.03554] μm, and the microscopic heterogeneity parameter is η = 0.4952; and for the randomly allocated network, the heterogeneity parameter is η = 0.9892.

For subnetwork extraction from a parent network with network size 31 containing fractures along the measurement direction (Figure 19), at the same subnetwork size, the relative deviation of the extraction results from fracture networks is substantially greater than that from networks with randomly assigned pore types. As the number of included fracture nodes increases, this deviation gradually decreases; however, after reaching a sufficiently large size (l = 10), a larger number of fracture nodes no longer implies a smaller

relative deviation. Fracture nodes refer to the selected nodes whose connected PC units were assigned relatively large pore radii.

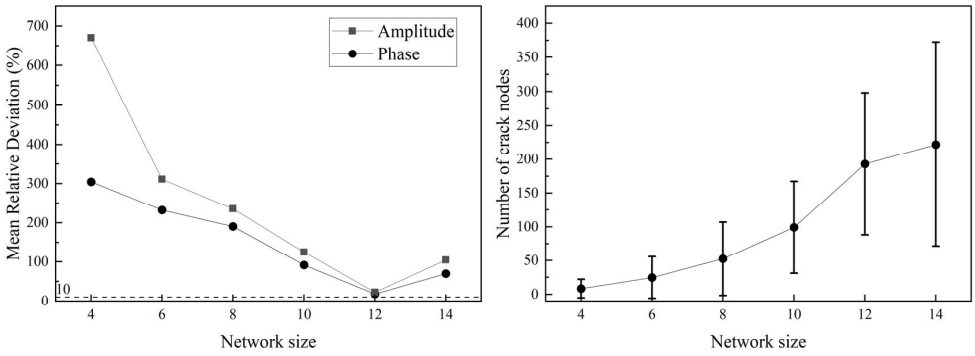


Figure 19. Panel (**a**) is mean relative deviation of subnetworks of different sizes, with parent network parameters same as in Figure 8, and (**b**) is number of crack nodes contained in different subnetwork sizes.

The fracture node proportions of subnetworks with minimum relative deviation cluster near the fracture node proportion of the parent network (Figure 20). The relative deviations in magnitude and phase for subnetworks of the same size vary nonlinearly with the number of fracture nodes (Figure 21). Because the spatial distribution of fractures differs in each subnetwork, subnetworks with identical fracture node proportions can exhibit relative deviations differing by several-fold. In Figure 21, the two subnetworks with the minimum relative deviation share similar pore throat distributions. When the parent network exhibits large-scale heterogeneity, subnetwork representativeness depends not only on sampling sufficiency but also on similarity to the parent network; rather, the subnetwork must maintain self-similarity with the parent network in fracture structure, such that both the fracture node proportion and the spatial distribution pattern are consistent with those of the parent network.

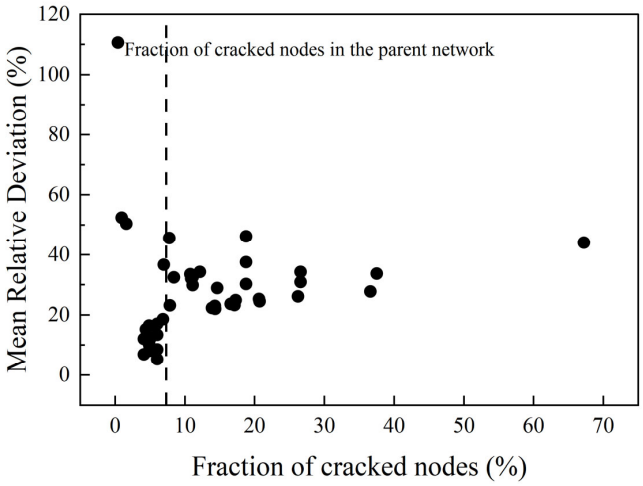


Figure 20. Average relative deviations in resistivity magnitude and phase for all subnetwork sizes across 10 extraction iterations, plotted against the corresponding fracture node proportions. Data points for subnetworks containing no fracture nodes were excluded from the comparison because their relative deviations exceeded tenfold, which would obscure the distribution of the remaining data.

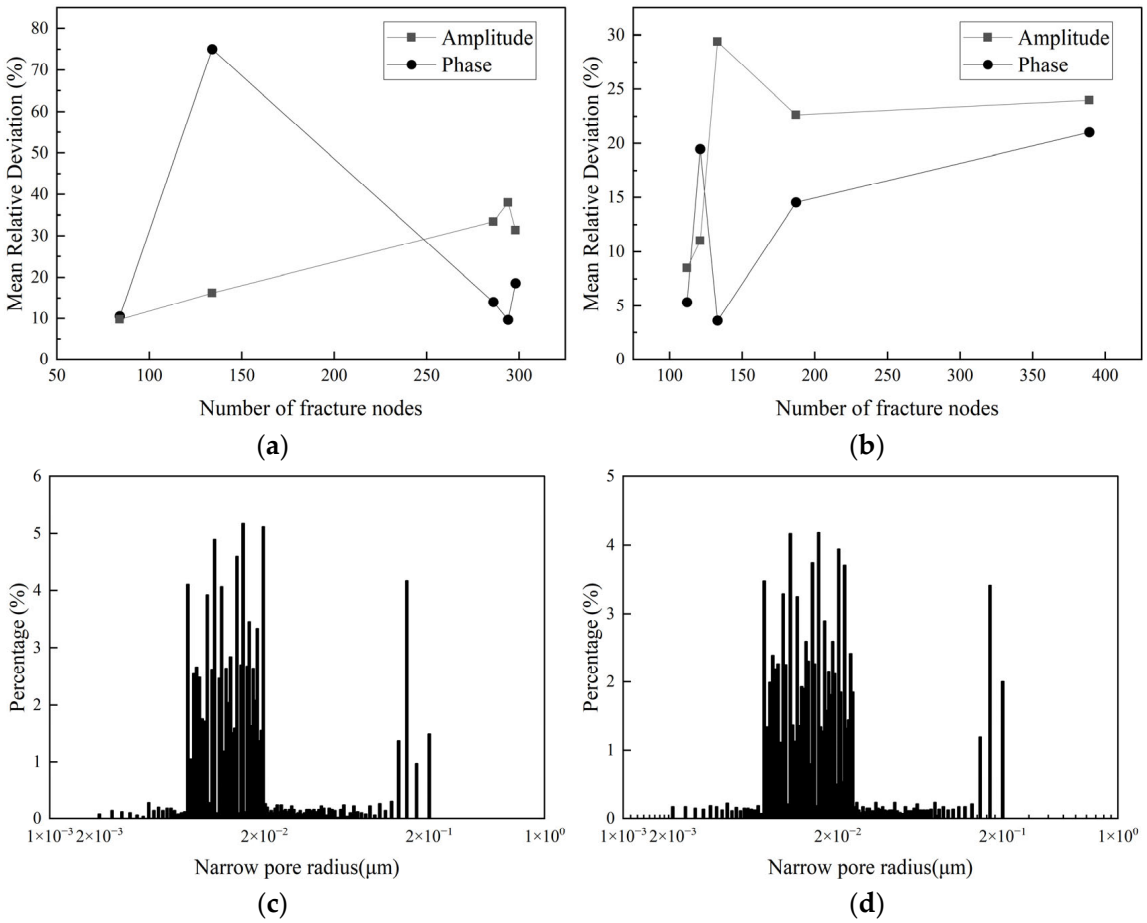


Figure 21. Relative changes in amplitude and phase for subnetworks of sizes 12 and 14 under different numbers of fracture nodes (**a**,**b**); (**c**,**d**) show the pore size distributions of the two networks with the smallest relative changes.

Further considering spatial correlation, fracture branches perpendicular to the measurement direction were added to the fractures along the measurement direction to simulate more complex fracture networks (Figure 22), serving as a transition from idealized fractures to natural fracture networks. The average deviation of the subnetwork SIP response relative to the parent network increases (Figure 23); however, as the subnetwork size increases, the average relative deviation of the subnetworks shows no convergence trend. The average relative deviation of a subnetwork with network size 20 occupying 2/3 of the parent network volume is almost indistinguishable from that of a subnetwork with network size 8. The correlation between the subnetwork relative deviation magnitude and the fracture node proportion weakens. Relative to a parent network containing only fractures along the measurement direction, small-size subnetworks can hardly achieve sufficient spatial similarity with a parent network possessing complex fracture networks. To attain self-similarity, the extracted subnetwork size must be comparable to that of the parent network. At the core scale, for large-scale cores with strong heterogeneity, the representativeness of SIP measurements on standard plug sample sizes is significantly reduced or even lost. Whether such core-scale heterogeneity extends to larger scales (e.g., logging resolution) requires verification using imaging data.

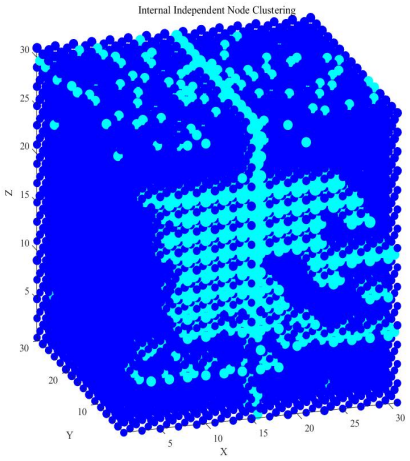


Figure 22. Addition of branch layers perpendicular to the fractures, based on the fractures along the measurement direction in Figure 18. Dark-blue and cyan nodes represent the small-pore and large-pore/fracture-node classes, respectively.

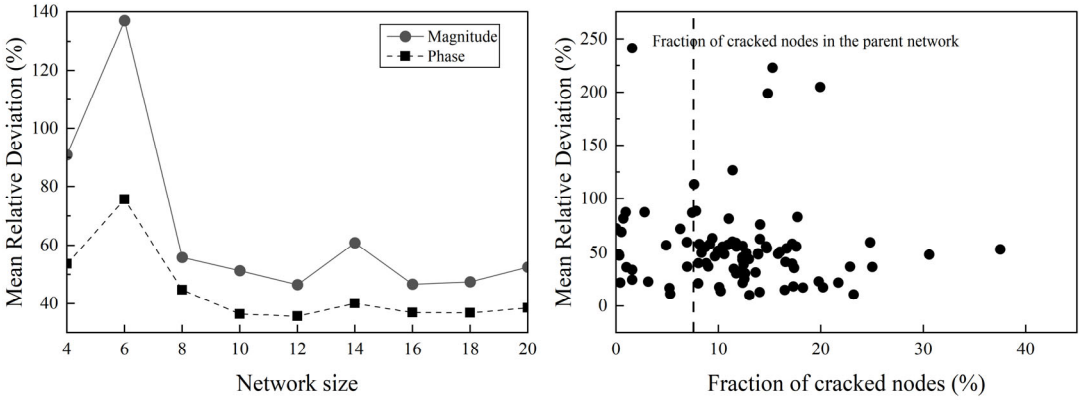


Figure 23. (**a**) Average relative deviations of SIP responses for subnetworks of different sizes over 10 extraction iterations; parent network parameters are the same as in Figure 19. (**b**) Average relative deviations in resistivity magnitude and phase for all subnetwork sizes extracted over 10 iterations, plotted against the corresponding fracture node proportions.

3.3. Application to Actual Samples

3.3.1. Measurement Instrument, Validation, and Data Selection

A Solartron 1260A impedance/gain-phase analyzer (Solartron Analytical, AMETEK Scientific Instruments, Farnborough, UK) was used for the complex resistivity measurements over the frequency range of 0.01–10,000 Hz. The rock samples were measured using the four-electrode configuration shown in Figure 24, with the outer electrodes used for current injection and the inner electrodes used for potential measurement. The analyzer and measurement system were connected to a common ground and electromagnetically shielded to reduce external electromagnetic interference. Nevertheless, recent studies have shown that broadband four-electrode SIP measurements may still be affected by acquisition-channel capacitance, potential-electrode and contact impedances, and electromagnetic coupling at elevated frequencies [52–54]. Therefore, before measuring the rock samples, we quantitatively evaluated the magnitude and phase accuracy of the analyzer over the investigated frequency range using phase-bearing reference networks. Analytical-reagent-grade $CuSO_4 \cdot 5H_2O$ (Karan, Xi'an Tianmao Baoding Biotechnology Co., Ltd., Xi'an, China) was used to prepare the $CuSO_4$ paste for electrode contact.

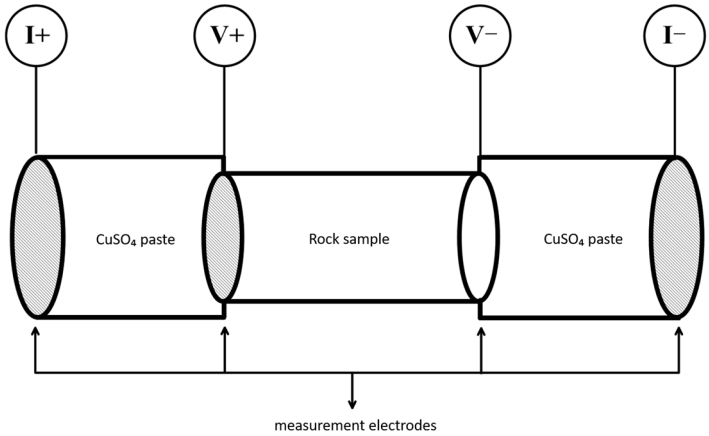


Figure 24. Schematic of the four-electrode configuration used for complex resistivity measurements. The outer electrodes (I+ and I−) were used for current injection, whereas the inner electrodes (V+ and V−) were used to measure the potential difference. $CuSO_4$ paste was used as the coupling medium between the electrodes and the rock sample.

Three phase-bearing R–C reference networks were used for the instrumental validation, and their circuit parameters are listed in Table 5. The measured and theoretical responses over the complete measurement band are compared in Figure 25. The relative residuals between the measured and theoretical responses remained below 5% for both impedance magnitude and phase. Representative residuals at 10, 100, 1000, and 10,000 Hz for the three R–C reference networks are summarized in Table 6. No separate open- or short-circuit compensation was applied; instead, the instrumental response was evaluated directly using the phase-bearing R–C loads. These reference measurements were used to quantify the instrumental measurement error rather than to derive a correction coefficient, and no frequency-dependent numerical correction was subsequently applied to the measured rock spectra.

Table 5. Circuit parameters of the three R–C reference networks used for instrumental validation.

Number	R_1/(kΩ)	R_2/(kΩ)	C/(μF)	φ_{max}/(rad)
R–C 1	20.00	0.2	68	0.005
R–C 2	1.900	0.2	68	0.050
R–C 3	0.108	0.2	68	0.500

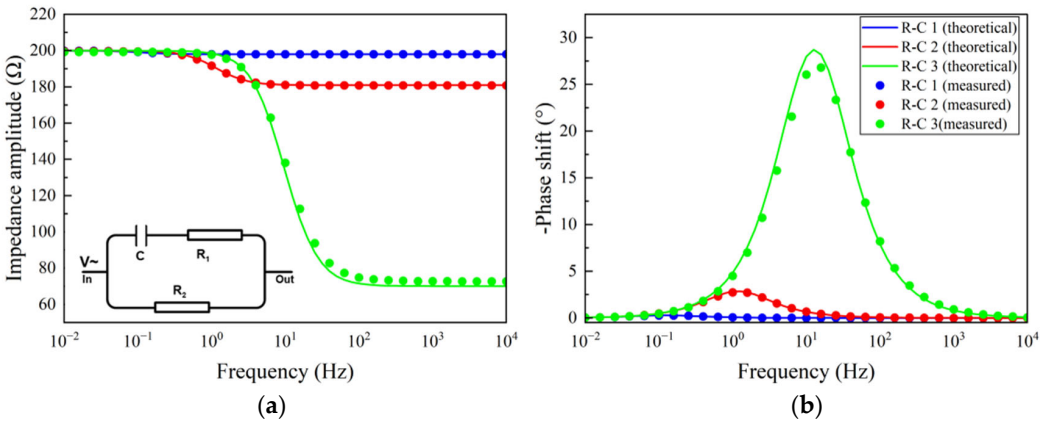


Figure 25. Validation of the impedance analyzer using three phase-bearing R–C reference networks. (**a**) Measured and theoretical impedance magnitudes. The inset in panel (**a**) shows the R–C reference circuit. (**b**) Measured and theoretical phase responses. Symbols represent the measurements, and solid curves represent the theoretical responses.

Table 6. Relative residuals of the impedance magnitude and phase measured for the three R–C reference networks at representative frequencies.

Number	Frequency (Hz)	Magnitude Relative Residual (%)	Phase Relative Residual (%)
R–C 1	10	0.0201	1.0009
	100	0.0001	1.0383
	1000	0.0102	1.3264
	10,000	0.0051	4.4422
R–C 2	10	0.0787	1.0537
	100	0.0788	3.0011
	1000	0.0691	0.0064
	10,000	0.0542	0.0272
R–C 3	10	3.6159	0.0715
	100	3.7180	0.1339
	1000	4.4897	0.0380
	10,000	3.4984	0.0748

It is important to distinguish the acquisition frequency range from the frequency range used in the impedance network inversion. Although the complete measured spectra up to 10 kHz are presented for transparency, the adopted pore throat model describes electrochemical polarization associated with ion redistribution and the coupled polarization of the Stern and diffuse layers. It does not contain an explicit bulk-dielectric or Maxwell–Wagner polarization term. Consequently, the high-frequency dielectric-polarization segment was excluded from the inversion and was not included in the objective function. Only the lower-frequency electrochemical-polarization response was inverted using the impedance network model. The measured frequency range and the frequency range used for the inversion of each rock sample are listed in Table 7. Measured data outside the listed inversion ranges were excluded from the objective function. The excluded high-frequency data were neither corrected nor fitted and were not interpreted in terms of pore geometry. The need to separate the induced polarization response from high-frequency trends associated with dielectric behavior and/or electromagnetic noise has also been recognized in recent three-dimensional impedance network modeling [34].

Table 7. Frequency ranges used for the impedance network inversion of the measured rock spectra.

Sample	Measured Frequency Range (Hz)	Frequency Range Used for Inversion (Hz)
C1	0.01–10,000	0.01–1000
C2	0.01–10,000	0.01–1000
y	0.01–10,000	0.01–1000
y1	0.01–10,000	0.01–100
y2	0.01–10,000	0.01–100

3.3.2. Simulation of Measured Data from Core Plug Samples

To match the pore structure of real rock samples, the geometric parameters of PC units must be set according to actual rock physical measurement data. Carbonate samples C1 and C2 were saturated with a 0.1 mol/L NaCl solution. Analytical-reagent-grade NaCl (Karan, Xi'an Tianmao Baoding Biotechnology Co., Ltd., Xi'an, China) was used to prepare the brine for saturating the rock samples. Sample C2 exhibits strong homogeneity, while sample C1 contains large-scale fractures. The complex resistivity of the samples is measured using an impedance analyzer, and mercury injection experiments are conducted to determine the pore throat distribution. The distribution of pore throat radius r_2 is described based

on mercury injection capillary pressure (MICP) data. The measured data of the samples are shown in Figure 26. The pore-size distributions were obtained by mercury intrusion capillary pressure (MICP) measurements using a PoreMaster 60 GT mercury intrusion porosimeter (Quantachrome Instruments, Boynton Beach, FL, USA).

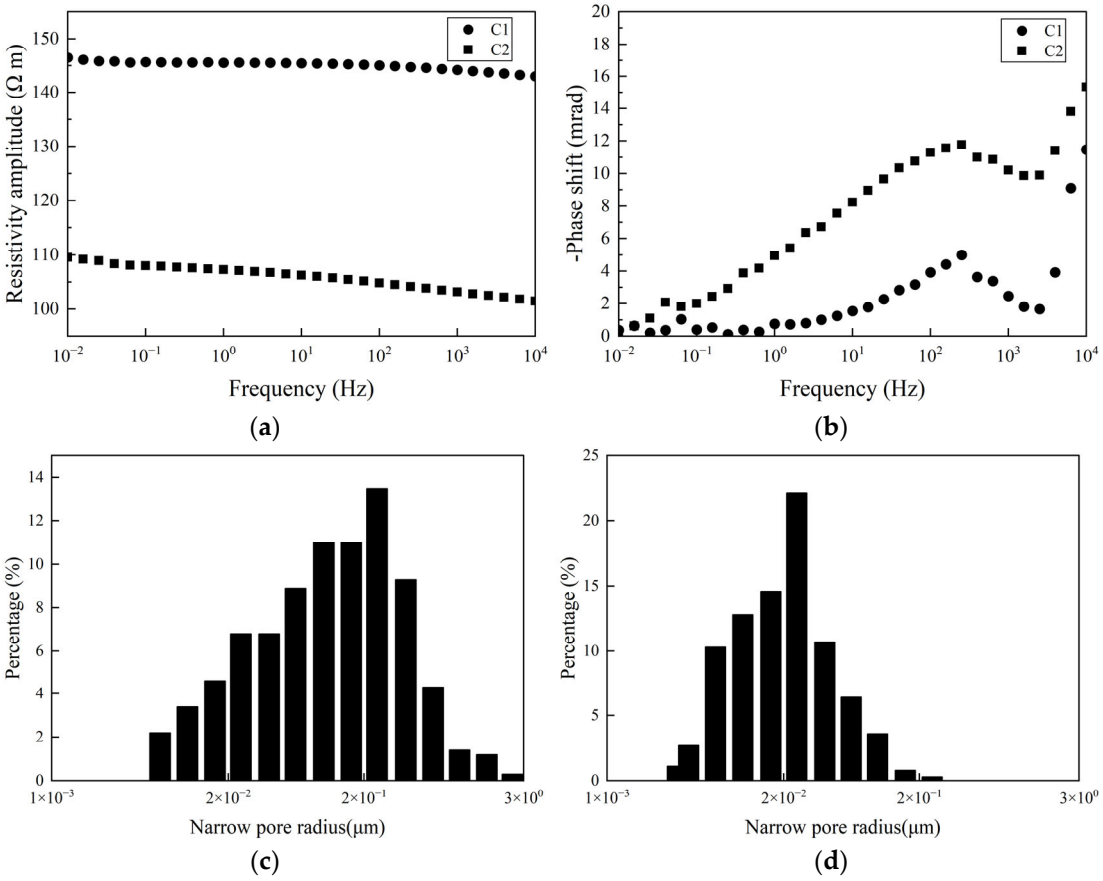


Figure 26. Panels (**a**,**b**) show the complex resistivity spectrum data of two measured samples, (**c**) shows the pore throat distribution of sample C1, and (**d**) shows the pore throat distribution of sample C2.

Fifty pore types were generated by interpolating the measured pore throat radius distribution. The narrow pore length is obtained through code optimization to match the characteristic frequency. The SIP response is simulated on a network with a scale of 24 (Figure 27). The simulated resistivity amplitudes of the impedance networks for samples C1 and C2 are both larger than the measured results. This discrepancy arises from the mismatch between the network and the actual sample porosity, as the pore throat probability distribution does not include the porosity information of the samples. The simulated resistivity phase of sample C1 is far lower than the measured data. Based on the simulation results, the existing pore throat distribution cannot provide the polarization intensity required by the measured data. Considering the unnatural truncation of the pore throat distribution at low pore sizes and the strong heterogeneity of sample C1, it may contain narrow pore distributions beyond the mercury injection measurement range to provide stronger polarization.

The error between the impedance network simulation results of pore types obtained through Bayesian optimization and the measured data is below 5% (Figure 28). The pore throat distribution of sample C2 is similar to the measured MICP results, where most small pores contributing to the resistivity amplitude are removed, which leaves only the main peak to match the amplitude and phase. The pore type distribution optimized for sample C1

lies at the truncation point of the measured mercury injection data. To match the measured SIP response of C1, Bayesian optimization introduces additional narrow pore types in the truncated region (Figure 28c). It predicts that C1 contains a group of narrow pores below the lower detection limit of mercury injection that provide strong polarization. This prediction is consistent with the geological understanding of clay filling or micropore development commonly found in fractures, but it requires further verification through independent micropore characterization methods such as low-temperature nitrogen adsorption or FIB-SEM (Focused Ion Beam Scanning Electron Microscopy).

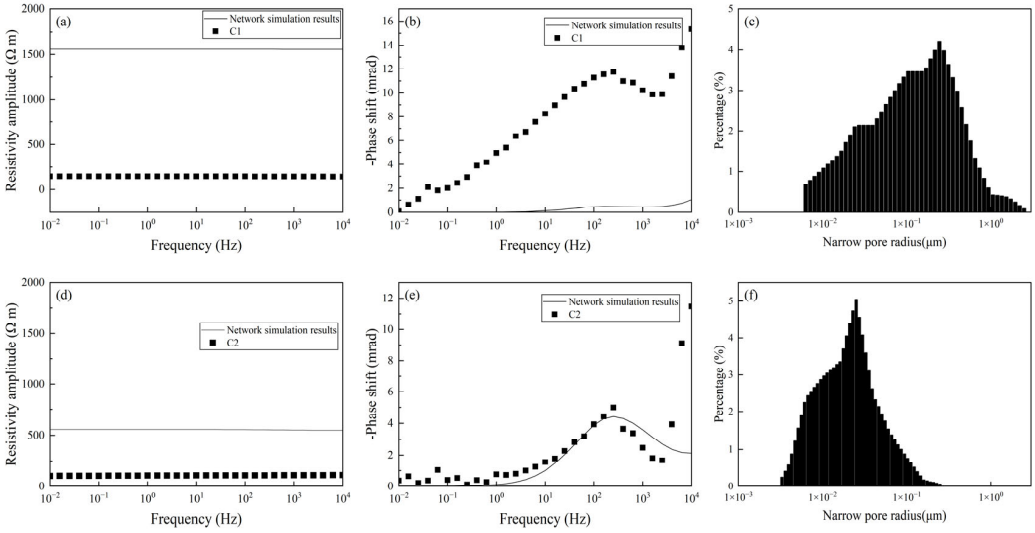


Figure 27. We interpolated the MICP distributions from samples C1 and C2 to construct 50 pore types and simulated them with the impedance network model. Panels (**a**–**c**) show the results for sample C1—resistivity amplitude, phase, and pore throat distribution—in that order. Panels (**d**–**f**) present the corresponding outputs for sample C2. Solid curves denote the network simulations; scatter points mark the experimental data.

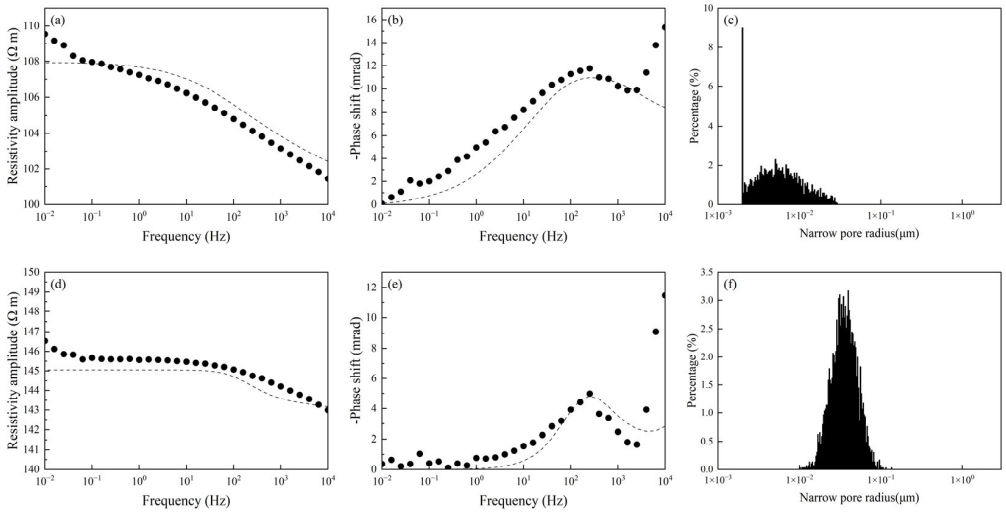


Figure 28. Using Bayesian optimization, we constructed pore types and simulated them with the impedance network model. Panels (**a**–**c**) show the results for sample C1 (81 pore types): resistivity amplitude, phase, and pore throat distribution, respectively. Panels (**d**–**f**) give the corresponding outputs for sample C2 (100 pore types), in the same order. Scatter points are experimental data; curves show the simulation results. Only data within the sample-specific inversion ranges listed in Table 7 were included in the inversion; higher-frequency measurements are shown only to present the complete experimental spectra.

3.3.3. Comparison of Induced Polarization Responses of Block Sample and Its Parts

A block sandstone sample, S03-3k, was saturated with a 0.1 mol/L NaCl solution, and its complex resistivity was measured along the x, y, and z directions. The measurement results are shown in Figure 29. The block sample has a long fracture perpendicular to the z measurement direction (Figure 29).

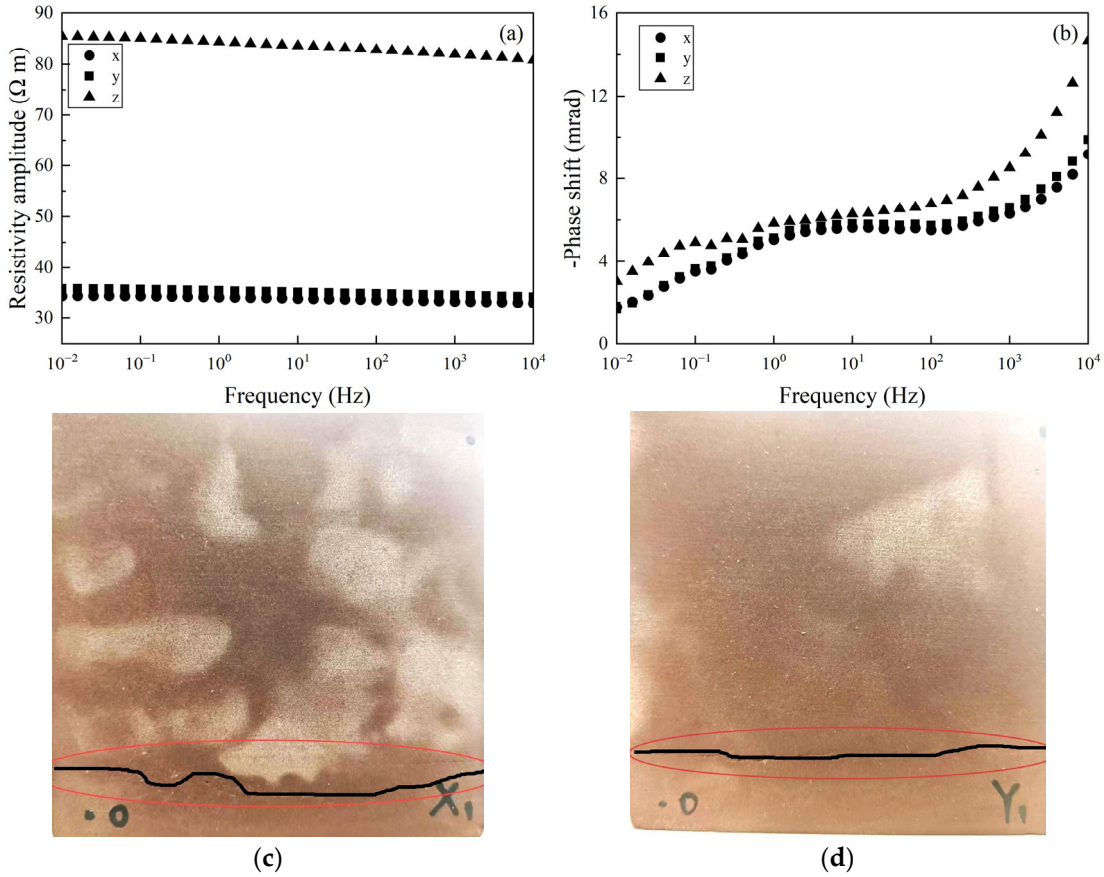


Figure 29. Panels (**a**,**b**) show resistivity amplitude and phase spectrum data for block sample S03-3k, with x, y, and z indicating results from different measurement directions; (**c**) denotes the measurement direction along the *x*-axis; and (**d**) denotes the measurement direction along the *y*-axis. The red outlines in panels (**c**,**d**) indicate the visible fracture traces.

Measurements along the fracture direction show a more pronounced low-frequency polarization and significantly lower resistivity amplitude compared to those perpendicular to the fracture. Plug samples x1, x2, y1, y2, z1, z2, and z3 were drilled from the block sample in each measurement direction, among which sample y1 contains a long fracture running through both ends of the plug. Complex resistivity measurements were performed on all samples (Figure 30).

The SIP response deviation of sample y1 relative to the y direction measurement is much greater than that of sample y2 and plug samples in the other directions, because the presence of through-going fractures in sample y1 makes its spatial similarity with the block sample much worse than that of relatively homogeneous samples. Unlike previous numerical simulation results, large-scale fractures in block sample S03-3k constitute only a small fraction of its total volume.

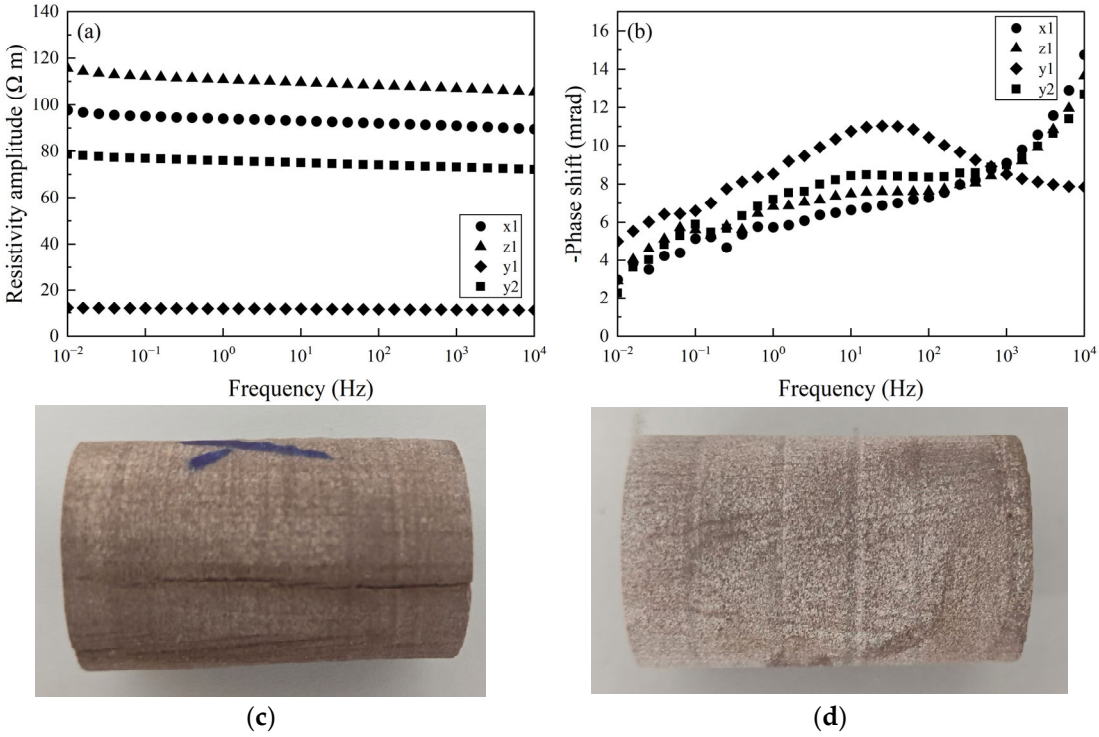


Figure 30. Panels (**a**,**b**) show the resistivity amplitude and phase spectrum data of different plug samples. The differences among samples x1–x2 and z1–z3 are less than 5%, so only one curve is plotted for each group. Panel (**c**) represents sample y1, and (**d**) represents sample y2.

Comparing the measurement results of the block sample and plug samples in the y direction, the fracture part contributes both lower resistivity amplitude and stronger polarization. Sample y1 shows a phase maximum, and the phase variation among y1-y2-y samples is similar to the results of the two pore types in Section 3.1: the phase peak corresponding to sample y1 is gradually flattened to that of sample y by progressively increasing the large-pore type. The lower resistivity amplitude is due to the fracture directly penetrating both ends of sample y1, providing an additional conductive path. Impedance network simulations were performed on y, y1, and y2 to obtain pore type distributions matching the measured data (Figures 31 and 32). The simulated pore type distributions of the three samples correspond to a gradual reduction in narrow pores from y1 to y2 to y.

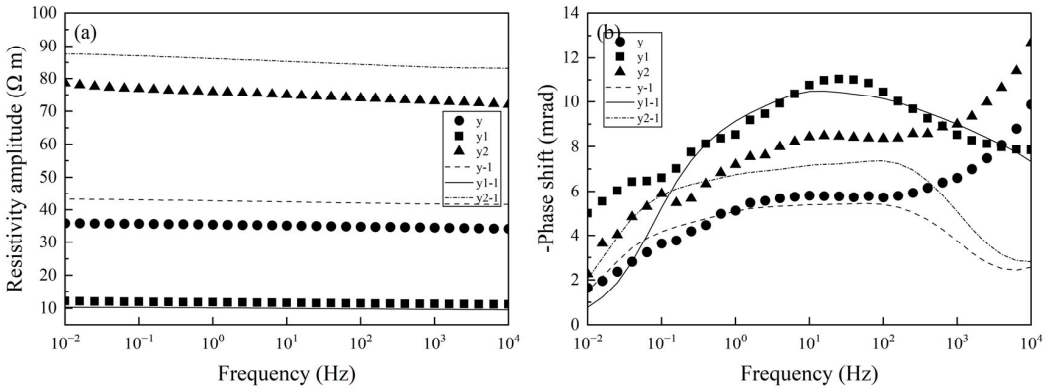


Figure 31. Panels (**a**,**b**) display complex resistivity spectra and impedance network simulation results for block and cylindrical samples in the same measurement direction. The dots represent the actual data, while the lines represent the simulated data. Only data within the sample-specific inversion ranges listed in Table 7 were included in the inversion; higher-frequency measurements are shown only to present the complete experimental spectra.

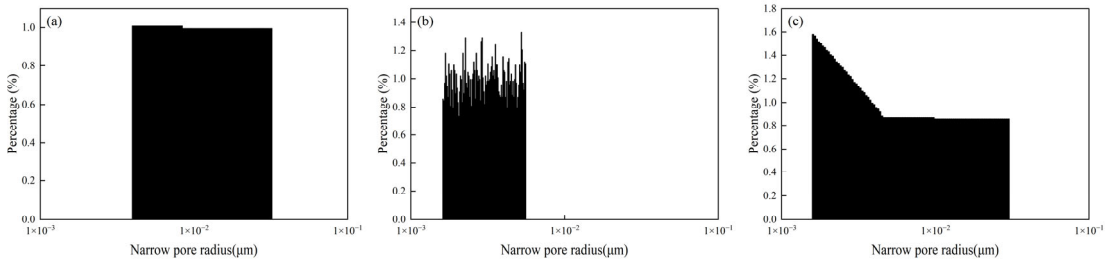


Figure 32. Pore throat distributions obtained from random impedance network model inversion for samples y, y1, and y2. (**a**) Pore throat distribution of sample y; (**b**) pore throat distribution of sample y1; (**c**) pore throat distribution of sample y2.

4. Discussion

Several closely related studies provide the methodological basis for the present work but address different scale problems. Stebner et al. [31] incorporated pore-scale membrane polarization responses into impedance networks to obtain bulk effective SIP spectra, whereas Maineult et al. [32] used random tube networks with phenomenological Pelton elements for comparable pore-to-bulk upscaling. These 2017 studies, therefore, established the use of impedance networks to connect microscopic polarization units to macroscopic effective responses. Kreith et al. [24] subsequently developed the improved pore throat electrochemical formulation adopted in the present study by explicitly accounting for Stern-layer cations in the coupled ionic-transport equations. The present study adopts this formulation and does not introduce a new membrane polarization equation. More recently, Maineult et al. [34] used three-dimensional resistor–leaky-capacitor networks to reproduce sample-scale spectra of sand–pyrite–water mixtures and to relate macroscopic Pelton parameters to pyrite-associated network elements. By contrast, the present study focuses on nonmetallic tight-reservoir pore–fracture systems and introduces a second upscaling stage—from a local core subvolume represented by a subnetwork to a larger parent core. The additional contribution lies in evaluating scale-dependent representativeness through REV determination, repeated subnetwork extraction, spatially correlated fracture configurations, structural self-similarity, and block-to-plug experimental comparison.

The impedance network model adopted in this study involves idealized simplifications in both geometric structure and electrochemical parameters, which limit its ability to accurately reproduce the microstructure of natural tight reservoirs. First, the distribution of pore types is optimized under prescribed statistical assumptions. The fixed proportional relationships between pore bodies and pore throats also restrict the range of pore geometries that can be represented, and other pore type combinations may reproduce the measured SIP spectra equally well. Second, uniform electrochemical parameters are assigned to all pore types, which does not reflect the mineral-surface heterogeneity of natural rocks; variations in surface charge density and Stern-layer properties among different minerals may lead to substantial differences in polarization magnitude and in the pore sizes that contribute to the SIP response [55]. Furthermore, the representation of large-scale fractures remains simplified. In the present model, fractures are approximated by spatially clustering PC units with relatively large pore radii, while each network edge is treated as an independent impedance element. Consequently, electrochemical coupling between adjacent edges and the possible continuity of the electrical double layer along natural fracture surfaces are not represented. Previous numerical studies have shown that system-scale EDL interconnection can substantially enhance diffuse-layer polarization and make its contribution comparable to that of Stern-layer polarization [23]. Therefore, the present fracture representation may underestimate the SIP response associated with large-scale fractures. These geometric and electrochemical simplifications constrain the applicability of the network model un-

der complex geological conditions. Future work will first address these limitations by improving the network geometry, rock-specific electrochemical calibration, experimental validation, and inversion constraints. On this basis, inter-edge electrochemical coupling and system-scale EDL continuity along large fractures will be investigated to determine how fracture length, connectivity, and EDL continuity affect the SIP response.

In the simulated core-scale networks, the introduction of large-scale fractures, dissolution pores, and other heterogeneous structures causes SIP responses to exhibit significant non-local characteristics. The numerical results suggest that, for parent networks containing large-scale fractures, subnetwork representativeness may depend on the similarity of the fracture proportion and spatial distribution between the local and parent volumes. From the perspective of multiscale porous-media theory [56], continuous hierarchical heterogeneity may introduce non-local effects into macroscopic transport. Consequently, conventional plug-scale measurements based on a local REV assumption may not fully capture the long-range electrical influence of large fractures. Moreover, plug samples are often collected from visually homogeneous portions of fractured block or full-diameter cores, which may cause laboratory SIP measurements to underrepresent larger-scale fracture-related heterogeneity. Whether such core-scale heterogeneity persists and affects SIP responses at the logging scale remains uncertain and requires verification using logging data. These findings suggest potential implications for laboratory sampling and the scale extrapolation of SIP measurements. For relatively homogeneous cores, increasing the sample volume beyond the REV tends to improve the stability of the measured response. For strongly heterogeneous fractured cores, however, representativeness may depend not only on sample size but also on how well the sampled volume captures the fracture proportion, orientation, connectivity, and spatial distribution of the parent core. SIP measurements obtained from visually homogeneous plug samples may, therefore, underrepresent fracture-related electrical pathways, and their extrapolation to full-diameter cores or logging scales should be treated with caution unless supported by core images, computed tomography, or logging data. In addition, pore size distributions obtained by impedance network inversion are more appropriately regarded as electrically equivalent descriptions rather than unique reconstructions of the actual pore structure.

Impedance network inversion is essentially an electrical equivalent characterization technique, and the process of inverting the pore structure from measured SIP spectra inherently involves irreducible non-uniqueness, with no unique correspondence between the inverted pore type distribution and the actual petrophysical structure. Specifically, the inversion uses the measured SIP amplitude and phase spectra as objective functions and employs Bayesian optimization to search for the pore type combination that minimizes the discrepancy between the simulated and measured spectra; however, for a strongly heterogeneous fractured sample like C1, the optimized pore throat distribution differs significantly from the mercury injection measured distribution. The algorithm predicts a large number of narrow pores at the mercury injection cutoff to match the polarization intensity, but the large pores at the mercury injection measured location completely disappear. This discrepancy stems from two factors: on the one hand, the aforementioned model simplifications—including geometric distribution assumptions, fixed proportionality coefficients, and the homogenization of electrochemical parameters—severely compress the inversion solution space, making it possible for different pore combinations to produce similar spectral responses; on the other hand, inverting microscopic pore structure using macroscopic SIP response as a constraint is inherently ill posed. Electrical measurements are sensitive to narrow pore polarization structures, while seepage measurements such as mercury injection are sensitive to large-pore seepage channels. For heterogeneous samples where these two structures coexist in large numbers, a single-scale statistical distribution

of pore throats encounters difficulty in constraining both physical properties simultaneously. As Gomaa and Kassab [57] pointed out, in PRNG (Pseudo-Random Renormalization Group) inversion, fitting macroscopic electrical responses often involves local minima and non-uniqueness in the parameter space, and different pore combinations may produce similar spectral responses. Therefore, the existing impedance network inversion essentially seeks an equivalent pore combination in the electrical response space, and its inversion results lack independent experimental verification. It should not be directly used as a basis for quantitative rock physics interpretation but rather be regarded as an electrical equivalent characterization technique. Future inversion studies will incorporate imaging constraints and rock-specific electrochemical calibration to reduce solution non-uniqueness and improve the physical interpretability of the recovered pore distributions.

5. Conclusions

This study established a cross-scale characterization method based on an improved membrane polarization model and a three-dimensional impedance network. We solved the coupled Poisson–Nernst–Planck equations to obtain pore-scale complex impedance and upscaled the response to the core scale via Kirchhoff's law. We analyzed the relationship between global and local SIP responses at the core scale in tight reservoirs. The numerical experiments indicate that the induced polarization response of microscopically heterogeneous rocks is primarily controlled by the distribution ranges of narrow pore radius and pore length. Under log-normal or uniform distribution conditions, the representative elementary volume (REV) of such rocks increases with the broadening of pore radius and pore length distributions. For strongly heterogeneous rocks containing macroscopic fractures and dissolution pores, the validity of the REV is challenged.

For strongly heterogeneous cores, random sampling may fail to provide effective characterization of the whole. The present numerical experiments indicate that, when a subnetwork lacks sufficient spatial similarity to the parent network, the relative deviation in its SIP response can exceed tenfold. For large-scale tight cores that are strongly heterogeneous and exhibit connected, clustered fracture distributions, the representativeness of small-scale core SIP measurements may decrease significantly.

With respect to inversion validity, existing impedance network optimization results are less effective for strongly heterogeneous samples and require additional constraints such as porosity. For relatively homogeneous samples, although inversion can yield pore throat distributions comparable to measured data, the inversion results represent only an electrical equivalent characterization rather than a unique reconstruction of the true pore structure, owing to incomplete sample information and the non-uniqueness of response fitting. Their interpretation should be limited to spectral response matching and should not be directly extrapolated as quantitative rock physics interpretations.

The present framework remains subject to several limitations. The idealized network geometry, prescribed relationships between pore bodies and pore throats, and uniform mineral–electrochemical parameters cannot fully reproduce the complex pore topology and mineral-surface heterogeneity of natural rocks. The inversion is also intrinsically non-unique, and the current experimental validation covers only a limited range of core samples. Moreover, large-scale fractures are presently approximated by spatially clustering PC units with relatively large pore radii, while individual network edges are treated as independent impedance elements. Consequently, electrochemical interactions between adjacent edges and the possible continuity of the electrical double layer along natural fracture surfaces are not represented, which may lead to an underestimation of fracture-related polarization. Future work will first improve the network geometry, rock-specific electrochemical calibration, experimental validation, and inversion constraints. On this

basis, inter-edge electrochemical coupling and system-scale EDL continuity along large fractures will be investigated to determine how fracture length, connectivity, and EDL continuity affect the SIP response.

Author Contributions: Conceptualization, T.W. and X.T.; methodology, T.W.; software, T.W.; validation, T.W., K.X. and X.T.; formal analysis, T.W.; investigation, T.W.; resources, T.W.; data curation, T.W.; writing—original draft preparation, T.W.; writing—review and editing, X.T. and K.X.; visualization, T.W.; supervision, K.X.; project administration, K.X.; funding acquisition, L.Y. All authors have read and agreed to the published version of the manuscript.

Funding: This research was funded by the National Natural Science Foundation of China (Grant Nos. 42574100 and 42530809), Deep Earth Probe and Mineral Resources Exploration—National Science and Technology Major Project (2025ZD1008903), and the scientific and technological project of China National Petroleum Corporation: Research on Joint Monitoring and Evaluation Method of Multi-Physical Fields for Oil and Gas Reservoirs (2023ZZ05-06).

Data Availability Statement: The data used to support the findings of the study are available from the first author upon request.

Conflicts of Interest: The authors declare no conflicts of interest.

Abbreviations

The following abbreviations are used in this manuscript:

EDL	Electrical double layer
FIB-SEM	Focused Ion Beam Scanning Electron Microscopy
IP	Induced polarization
MICP	Mercury injection capillary pressure
PC	Pore combination
PRNG	Pseudo-Random Renormalization Group
REV	Representative elementary volume
SCM	Surface complexation model
SIP	Spectral induced polarization

Appendix A

Statistical Criteria for REV Determination

For an impedance network with the i-th network size l_i, the simulated resistivity magnitude and phase at frequency f_h in the j-th realization are denoted by ρ_{ijh} and ϕ_{ijh}, respectively. Statistical stability among repeated realizations was evaluated using the coefficients of variation of resistivity magnitude and phase:

$$CV_\rho(l_i, f_h) = \frac{\sigma_\rho(l_i, f_h)}{\mu_\rho(l_i, f_h)} = \frac{\sqrt{\frac{1}{n-1}\sum_{j=1}^{n}(\rho_{ijh} - \overline{\rho}_{ih})^2}}{\frac{1}{n}\sum_{j=1}^{n}\rho_{ijh}} \tag{A1}$$

The corresponding coefficient of variation of the phase is defined as:

$$CV_\phi(l_i, f_h) = \frac{\sigma_\phi(l_i, f_h)}{|\mu_\phi(l_i, f_h)|} = \frac{\sqrt{\frac{1}{n-1}\sum_{j=1}^{n}(\phi_{ijh} - \overline{\phi}_{ih})^2}}{\left|\frac{1}{n}\sum_{j=1}^{n}\phi_{ijh}\right|} \tag{A2}$$

The full-band coefficients of variation were obtained by averaging the frequency-dependent coefficients over all N frequencies:

$$\overline{CV}_\rho(l_i) = \frac{\sum_{h=1}^{N} CV_\rho(l_i, f_h)}{N} \quad \overline{CV}_\phi(l_i) = \frac{\sum_{h=1}^{N} CV_\phi(l_i, f_h)}{N} \tag{A3}$$

To evaluate the disappearance of the size effect, the full-band mean resistivity magnitude and phase were first calculated for each network size. The relative changes between two consecutive network sizes, l_{i-1} and l_i, were then determined as follows:

$$\delta_\rho(l_i) = \frac{|\overline{\rho}(l_i) - \overline{\rho}(l_{i-1})|}{\overline{\rho}(l_{i-1})} \tag{A4}$$

$$\delta_\phi(l_i) = \frac{|\overline{\phi}(l_i) - \overline{\phi}(l_{i-1})|}{|\overline{\phi}(l_{i-1})|} \tag{A5}$$

where $\overline{\rho}(l_i) = \frac{1}{nN}\sum_{h=1}^{N}\sum_{j=1}^{n}\rho_{ijh}$, $\overline{\phi}(l_i) = \frac{1}{nN}\sum_{h=1}^{N}\sum_{j=1}^{n}\phi_{ijh}$ are, respectively, the full-band average amplitude and phase over all cycles for size l_i.

These statistical quantities were used jointly to determine the minimum network size at which both the inter-realization variability and the inter-size variation fell below the prescribed thresholds.

Appendix B

Definition of the Microscopic Heterogeneity Parameter

To quantify the microscopic heterogeneity of pore throat radii around individual nodes, a set of mutually nonadjacent nodes was selected from the network. This selection avoids repeated evaluation of the same connecting edges. For the i-th selected node, let r_{ij} denote the pore throat radius of its j-th connected edge, and let m_i be the number of edges connected to that node. The local coefficient of variation C_i is defined as:

$$C_i = \frac{\sigma_i}{\overline{r}_i} = \frac{\sqrt{\frac{1}{m_i}\sum_{j=1}^{m_i}(r_j - \overline{r}_i)^2}}{\overline{r}_i} \tag{A6}$$

where $\overline{r}_i$ and σ_i are the mean and standard deviation of the pore throat radii connected to node i, respectively.

The microscopic heterogeneity parameter η is then defined as:

$$\eta = \frac{1}{N_{\text{node}}}\sum_{i=1}^{N_{\text{node}}} \min\left(\frac{C_i}{C_{\max}}, 1\right) \tag{A7}$$

where N_{node} is the number of selected mutually nonadjacent nodes and $C_{\max}$ is the prescribed upper bound used to normalize the local coefficient of variation. A larger value of η indicates greater variability among the pore throat radii connected to the selected nodes and, therefore, stronger microscopic heterogeneity. This parameter characterizes local pore radius contrasts around independent nodes, rather than the large-scale spatial organization or long-range correlation of pore structures within the entire network.

References

1. Weller, A.; Breede, K.; Slater, L.; Nordsiek, S. Effect of Changing Water Salinity on Complex Conductivity Spectra of Sandstones. *Geophysics* **2011**, *76*, F315–F327. [CrossRef]
2. Revil, A. Spectral Induced Polarization of Shaly Sands: Influence of the Electrical Double Layer. *Water Resour. Res.* **2012**, *48*, W02517. [CrossRef]
3. Rigby, S.P.; Himona, E. Methods of Pore Structural Characterisation of Sedimentary Rocks and Their Constituent Minerals. *Minerals* **2024**, *14*, 756. [CrossRef]
4. Magoba, M.; Opuwari, M.; Liu, K. The Effect of Diagenetic Minerals on the Petrophysical Properties of Sandstone Reservoir: A Case Study of the Upper Shallow Marine Sandstones in the Central Bredasdorp Basin, Offshore South Africa. *Minerals* **2024**, *14*, 396. [CrossRef]
5. Wang, G.; Zhang, Q.; Shen, B.; Wang, P.; Du, W.; Wang, L.; Li, M.; Wan, C. Pore Structure and Fractal Characteristics of the Permian Shales in Northeastern Sichuan Basin, China. *Minerals* **2025**, *15*, 684. [CrossRef]
6. Chen, Z.; Zhang, J.; Yong, Z.; Ma, H. Tight Sandstone Reservoir Characteristics and Sand Body Distribution of the Eighth Member of Permian Shihezi Formation in the Longdong Area, Ordos Basin. *Minerals* **2025**, *15*, 463. [CrossRef]
7. Kemna, A.; Binley, A.; Slater, L. Crosshole IP Imaging for Engineering and Environmental Applications. *Geophysics* **2004**, *69*, 97–107. [CrossRef]
8. Binley, A.; Slater, L.D.; Fukes, M.; Cassiani, G. Relationship between Spectral Induced Polarization and Hydraulic Properties of Saturated and Unsaturated Sandstone. *Water Resour. Res.* **2005**, *41*, W12417. [CrossRef]
9. Titov, K.; Tarasov, V.; Ilyin, Y.; Seleznev, N.; Boyd, A. Relationships between Induced-Polarization Relaxation Time and Hydraulic Properties of Saturated Porous Media. *Geophys. J. Int.* **2010**, *180*, 1095–1106. [CrossRef]
10. Revil, A.; Karaoulis, M.; Johnson, T.; Kemna, A. Review: Some Low-Frequency Electrical Methods for Subsurface Characterization and Monitoring in Hydrogeology. *Hydrogeol. J.* **2012**, *20*, 617–658. [CrossRef]
11. Tong, M.; Li, L.; Wang, W.; Fan, Q.; Jiang, Y.; Zhang, J.; Ding, Z.; Cui, J. Estimation of Pore Size Distribution and Permeability of Shaly Sands from Induced Polarization Time Spectra. *Chin. J. Geophys.* **2005**, *48*, 710–716. [CrossRef]
12. Börner, F.D.; Schopper, J.R.; Weller, A. Evaluation of Transport and Storage Properties in the Soil and Groundwater Zone from Induced Polarization Measurements. *Geophys. Prospect.* **1996**, *44*, 583—601. [CrossRef]
13. Slater, L. Near-Surface Electrical Characterization of Hydraulic Conductivity: From Petrophysical Properties to Aquifer Geometries—A Review. *Surv. Geophys.* **2007**, *28*, 169–197. [CrossRef]
14. Revil, A.; Breton, M.L.; Niu, Q.; Wallin, E.; Haskins, E.; Thomas, D.M. Induced Polarization of Volcanic Rocks. 2. Influence of Pore Size and Permeability. *Geophys. J. Int.* **2017**, *208*, 814–825. [CrossRef]
15. Schwarz, G. A Theory of the Low-Frequency Dielectric Dispersion of Colloidal Particles in Electrolyte Solution. *J. Phys. Chem.* **1962**, *66*, 2636–2642. [CrossRef]
16. Leroy, P.; Revil, A.; Kemna, A.; Cosenza, P.; Ghorbani, A. Complex Conductivity of Water-Saturated Packs of Glass Beads. *J. Colloid Interface Sci.* **2008**, *321*, 103–117. [CrossRef] [PubMed]
17. Revil, A.; Florsch, N. Determination of Permeability from Spectral Induced Polarization in Granular Media. *Geophys. J. Int.* **2010**, *181*, 1480–1498. [CrossRef]
18. Niu, Q. Revisiting the Diffuse Layer Polarization of a Spherical Grain in Electrolytes with Numerical Solutions of Nernst-Planck-Poisson Equations. *J. Geophys. Res. Solid Earth* **2023**, *128*, e2022JB025934. [CrossRef]
19. Marshall, D.J.; Madden, T.R. Induced Polarization, a Study of Its Causes. *Geophysics* **1959**, *24*, 790–816. [CrossRef]
20. Bücker, M.; Hördt, A. Analytical Modelling of Membrane Polarization with Explicit Parametrization of Pore Radii and the Electrical Double Layer. *Geophys. J. Int.* **2013**, *194*, 804–813. [CrossRef]
21. Bücker, M.; Hördt, A. Long and Short Narrow Pore Models for Membrane Polarization. *Geophysics* **2013**, *78*, E299–E314. [CrossRef]
22. Revil, A. Low-Frequency Complex Conductivity of Sandy and Clayey Materials. *J. Colloid Interface Sci.* **2013**, *398*, 193–209. [CrossRef] [PubMed]
23. Bücker, M.; Flores Orozco, A.; Hördt, A.; Kemna, A. On the Role of Stern- and Diffuse-Layer Polarization Mechanisms in Porous Media. *J. Geophys. Res. Solid Earth* **2019**, *124*, 5656–5677. [CrossRef]
24. Kreith, D.; Leroy, P.; Bücker, M. A New Semi-Analytic Model for Stern-Layer Polarization in Pore Throats. *Geophys. J. Int.* **2024**, *239*, 1910–1927. [CrossRef]
25. Kirkpatrick, S. Percolation and Conduction. *Rev. Mod. Phys.* **1973**, *45*, 574–588. [CrossRef]
26. Koplik, J. On the Effective Medium Theory of Random Linear Networks. *J. Phys. C Solid State Phys.* **1981**, *14*, 4821–4837. [CrossRef]
27. David, C.; Gueguen, Y.; Pampoukis, G. Effective Medium Theory and Network Theory Applied to the Transport Properties of Rock. *J. Geophys. Res. Solid Earth* **1990**, *95*, 6993–7005. [CrossRef]
28. Man, H.N.; Jing, X.D. Pore Network Modelling of Electrical Resistivity and Capillary Pressure Characteristics. *Transp. Porous Media* **2000**, *41*, 263–285. [CrossRef]

29. Taghavinejad, A.; Rabbani, A.; Falcone, G.; Shang, J.; Arif, M.; Zhang, Y. Pore Network Modelling of CO_2-Shale Interaction for Carbon Storage: Swelling Effect and Fracture Permeability. *Int. J. Greenh. Gas Control* **2025**, *141*, 104294. [CrossRef]
30. Mufti, S.; Das, A. Pore Network Modeling Approach for Simulating Soil Water Retention Curve under Different Stress Conditions. *E3S Web Conf.* **2023**, *382*, 6. [CrossRef]
31. Stebner, H.; Halisch, M.; Hördt, A. Simulation of Membrane Polarization of Porous Media with Impedance Networks. *Near Surf. Geophys.* **2017**, *15*, 563–578. [CrossRef]
32. Maineult, A.; Revil, A.; Camerlynck, C.; Florsch, N.; Titov, K. Upscaling of Spectral Induced Polarization Response Using Random Tube Networks. *Geophys. J. Int.* **2017**, *209*, 948–960. [CrossRef]
33. Pelton, W.H.; Ward, S.H.; Hallof, P.G.; Sill, W.R.; Nelson, P.H. Mineral Discrimination and Removal of Inductive Coupling with Multifrequency IP. *Geophysics* **1978**, *43*, 588–609. [CrossRef]
34. Maineult, A.; Weller, A.; Martin, T.; Titov, K.; Florsch, N. 3-D Impedance Networks Simulate Complex Resistivity Spectra of Sand–Pyrite–Water Mixtures. *Geophys. J. Int.* **2025**, *242*, ggaf269. [CrossRef]
35. Leroy, P.; Hördt, A.; Gaboreau, S.; Zimmermann, E.; Claret, F.; Bücker, M.; Stebner, H.; Huisman, J.A. Spectral Induced Polarization of Low-pH Cement and Concrete. *Cem. Concr. Compos.* **2019**, *104*, 103397. [CrossRef]
36. Wu, C.; Zou, C.; Peng, C.; Liu, Y.; Wu, T.; Zhou, J.; Tao, C. Numerical Simulation Study on the Relationships between Mineralized Structures and Induced Polarization Properties of Seafloor Polymetallic Sulfide Rocks. *Minerals* **2022**, *12*, 1172. [CrossRef]
37. Eroshenko, A.A.; Lymar, I.V.; Khodkov, E.N. Experience of Applying Digital Core Technologies to Study Reservoir Rocks of the Pripyat Trough. *Georesources* **2026**, *28*, 119–132. [CrossRef]
38. Kadyrov, R.I.; Statsenko, E.O.; Nguyen, T.H.; Skorobogatova, M.A. Core Plug Porosity Prediction Using Microtomography, Supervised Labeling, and a Shifted Window Transformer. *Georesources* **2025**, *27*, 67–82. [CrossRef]
39. Bachmat, Y. Macroscopic Modelling of Transport Phenomena in Porous Media. 1: The Continuum Approach. *Transp. Porous Media* **1986**, *1*, 213–240. [CrossRef]
40. Zhang, D.; Zhang, R.; Chen, S.; Soll, W. Pore Scale Study of Flow in Porous Media: Scale Dependency, REV, and Statistical REV. *Geophys. Res. Lett.* **2000**, *27*, 1195–1198. [CrossRef]
41. Mostaghimi, P.; Bijeljic, B.; Blunt, M.J. Computations of Absolute Permeability on Micro-CT Images. *Math. Geosci.* **2012**, *44*, 103–116. [CrossRef]
42. Baveye, P.; Rogasik, H.; Wendroth, O.; Onasch, I.; Crawford, J.W. Effect of Sampling Volume on the Measurement of Soil Physical Properties: Simulation with X-Ray Tomography Data. *Meas. Sci. Technol.* **2002**, *13*, 775. [CrossRef]
43. Blunt, M.J.; Bijeljic, B.; Dong, H.; Gharbi, O.; Iglauer, S.; Mostaghimi, P.; Paluszny, A.; Pentland, C. Pore-Scale Imaging and Modelling. *Adv. Water Resour.* **2013**, *51*, 197–216. [CrossRef]
44. Al-Raoush, R.; Papadopoulos, A. Representative Elementary Volume Analysis of Porous Media Using X-Ray Computed Tomography. *Powder Technol.* **2010**, *200*, 69–77. [CrossRef]
45. Dvorkin, J.; Al-Mukainah, H.; Hussaini, S.R. Electrical Formation Factor versus Porosity Coarse-Scale Transforms from Microscopic Digital Images: Example-Based Study. *J. Pet. Sci. Eng.* **2022**, *210*, 110054. [CrossRef]
46. Keehm, Y.; Mukerji, T. Permeability and Relative Permeability from Digital Rocks: Issues on Grid Resolution and Representative Elementary Volume. In Proceedings of the 2004 SEG Annual Meeting, Denver, CO, USA, 10–15 October 2004; pp. 1654–1657. [CrossRef]
47. Lyklema, J.; Dukhin, S.S.; Shilov, V.N. The Relaxation of the Double Layer around Colloidal Particles and the Low-Frequency Dielectric Dispersion: Part I. Theoretical Considerations. *J. Electroanal. Chem. Interfacial Electrochem.* **1983**, *143*, 1–21. [CrossRef]
48. Bairlein, K.; Bücker, M.; Hördt, A.; Hinze, B. Temperature Dependence of Spectral Induced Polarization Data: Experimental Results and Membrane Polarization Theory. *Geophys. J. Int.* **2016**, *205*, 440–453. [CrossRef]
49. Leroy, P.; Devau, N.; Revil, A.; Bizi, M. Influence of Surface Conductivity on the Apparent Zeta Potential of Amorphous Silica Nanoparticles. *J. Colloid Interface Sci.* **2013**, *410*, 81–93. [CrossRef] [PubMed]
50. Leroy, P.; Tournassat, C.; Bernard, O.; Devau, N.; Azaroual, M. The Electrophoretic Mobility of Montmorillonite. Zeta Potential and Surface Conductivity Effects. *J. Colloid Interface Sci.* **2015**, *451*, 21–39. [CrossRef] [PubMed]
51. Leroy, P.; Maineult, A.; Li, S.; Vinogradov, J. The Zeta Potential of Quartz. Surface Complexation Modelling to Elucidate High Salinity Measurements. *Colloids Surf. A Physicochem. Eng. Asp.* **2022**, *650*, 129507. [CrossRef]
52. Garcia, A.; Slater, L. Spectral induced polarization laboratory measurements combining two and four-electrode measurement configurations. *Geophys. J. Int.* **2026**, *246*, ggag177. [CrossRef]
53. Zhang, H.; Chen, R.; Chun, S.; Xu, C. A New Calibration Method for Broadband Complex Resistivity Measurement System of Rocks and Ores. *Appl. Sci.* **2025**, *15*, 1526. [CrossRef]
54. Zimmermann, E.; Huisman, J.A. The effect of heterogeneous contact impedances on complex resistivity measurements. *Geophys. J. Int.* **2024**, *236*, 1234–1245. [CrossRef]
55. Chuprinko, D.; Titov, K. Influence of Mineral Composition on Spectral Induced Polarization in Sediments. *Geophys. J. Int.* **2017**, *208*, 186–191. [CrossRef]

56. Battiato, I.; Ferrero, V.D.O.; O'Malley, D.; Miller, C.T.; Takhar, P.S.; Valdés-Parada, F.J.; Wood, B.D. Theory and Applications of Macroscale Models in Porous Media. *Transp. Porous Media* **2019**, *130*, 5–76. [CrossRef]
57. Gomaa, M.M.; Kassab, M. Forward and Inverse Modelling of Electrical Properties of Some Sandstone Rocks Using Renormalisation Group Method. *Near Surf. Geophys.* **2017**, *15*, 487–498. [CrossRef]

Disclaimer/Publisher's Note: The statements, opinions and data contained in all publications are solely those of the individual author(s) and contributor(s) and not of MDPI and/or the editor(s). MDPI and/or the editor(s) disclaim responsibility for any injury to people or property resulting from any ideas, methods, instructions or products referred to in the content.